



Joint PP and PS pre-stack AVA inversion for VTI medium based on the exact Graebner equation

Cong Luo^a, Jing Ba^{a,*}, José M. Carcione^{a,b}, Guangtan Huang^c, Qiang Guo^d

^a School of Earth Sciences and Engineering, Hohai University, Nanjing, 211100, China

^b Istituto Nazionale di Oceanografia e di Geofisica Sperimentale (OGS), Borgo Grotta Gigante 42c, 34010, Sgonico, Trieste, Italy

^c School of Earth Sciences, Zhejiang University, Hangzhou, 310027, China

^d College of Information Engineering, China Jiliang University, Hangzhou, 310018, China

ARTICLE INFO

Keywords:

Pre-stack AVA inversion
Shale reservoir
VTI medium
Anisotropy parameters
Exact reflection coefficient
Multi-parameter

ABSTRACT

Unconventional hydrocarbon reservoirs, such as shale rocks, are generally transversely isotropic with a vertical axis of symmetry (VTI). The identification of sweet spots in these reservoirs, which must take into account this anisotropic character, can be performed with amplitude variations with offset/angle (AVO/AVA) inversion. However, most approaches use the Rüger reflection approximate equation as forward modeling, which has low accuracy at moderate to large angles, where the seismic gathers contain most of useful information on anisotropy parameters. In this paper, we propose an exact-equation-based seismic pre-stack AVA inversion for stable estimations of anisotropy parameters in VTI media. A linear inversion scheme is adopted to save computational time and the Fréchet derivatives, the key factors of the scheme, are derived here. To improve the stability and accuracy, the PP data inversion is extended to joint PP and PS inversion, termed joint exact-Graebner-based pre-stack inversion (JEGI). It is applied to both synthetic and field multi-component seismic data, showing its feasibility and effectiveness.

1. Introduction

Inversion algorithms use seismic data to obtain information about the geological formations, notably the presence of fluids related to hydrocarbons. For conventional hydrocarbon reservoirs, seismic inversion is generally based on the assumption of isotropic media. With the increasing demand for hydrocarbons, the exploration gradually moved to unconventional reservoirs (Ba et al., 2017; Ding et al., 2019; Pan et al., 2020), but in this case the media are anisotropic, as it is the case of shales (e.g., Carcione, 2000; Carcione et al., 2011).

Moreover, with a better understanding of subsurface media, it has been realized that the most crustal rocks are anisotropic (Thomsen, 1986). Among the various kinds of anisotropy, the VTI medium is one of the most common forms in hydrocarbon prospecting, mainly due to compaction, layering and intrinsic anisotropy, such as horizontal thin layers and textured shale (Zhang et al., 2019a). Further studies on a stable inversion method for this type of medium is meaningful to actual applications.

Previous studies reported that subsurface anisotropy has a significant influence on the seismic response (e.g., Wright, 1987). Thomsen (1986)

pointed out that most sedimentary rocks have weak anisotropy and proposed factors, known as Thomsen anisotropy parameters, to describe transverse isotropy, including media with a horizontal axis of symmetry (HTI). Using AVO/AVA algorithms, many studies are based on wave reflection coefficients for isotropic media as a function of the incidence angle and elastic properties (Aki and Richards, 1980; Shuey, 1985; Smith and Gidlow, 1987; Fatti et al., 1994; Zhang et al. 2015, 2019b; Karimpouli and Malehmir, 2015; Li et al., 2017; Liu et al., 2018; Guo et al., 2020; Guo et al., 2020). The case of TI media has also been studied (Daley and Hron, 1977), for instance, the reflection and transmission (RT) coefficients of SH waves (Daley and Hron, 1979). Kennett (1983), Kennett and Kerry (1979) and Fryer and Frazer (1984) proposed a reflectivity modeling (RM) based on an isotropic assumption to simulate propagation in a stratified medium and VTI media (Booth and Crampin, 1983; Mallick and Frazer, 1990). Graebner (1992) showed that the reflectivity methods are difficult to linearize and presented RT coefficients for two TI solids in welded contact. Carcione (1997, 2014) generalized the theory to anelastic TI media.

Many simplified RT coefficients have been used in AVO/AVA-related methods. For anisotropic media, the research focused on

* Corresponding author.

E-mail address: jba@hhu.edu.cn (J. Ba).

Table 1

Model 1 properties. P-wave velocity, S-wave velocity, density, and anisotropy parameters.

Layer	V_P (m/s)	V_S (m/s)	ρ (g/cm ³)	ϵ	δ
Top	3383	2438	2.35	0.12	0.059
Bottom	4237	3018	2.64	0.036	-0.039

approximations for TI media (Schoenberg, 1983; Thomsen, 1993; Ursin and Haugen, 1996; Rüger 1997, 1998; Vavryčuk and Pšenčík, 1998; Vavryčuk, 1999; Stovas and Ursin, 2003). The most commonly used PP- and PS-wave coefficients for pre-stack AVA inversion is the Rüger approximation (Rüger, 2002; Lu et al., 2018; Zhang et al., 2019a). In case that the simplified coefficients are provided, the inversion of amplitudes of reflected PP waves in VTI media is still difficult. The recovery of all five parameters is difficult in practice due to the issue of local minimum solutions in anisotropic AVO inversions (Plessix and Bork, 2000; Lee et al., 2010). The first problem of the existed VTI inversions is the limitation of the linearized approximations. Simplifications from exact equations in VTI media, similar to that of the isotropic case (Aki and Richards, 1980; Shuey, 1985; Smith and Gidlow, 1987; Fatti et al., 1994), are based on the assumption of weak contrasts and have low accuracy at medium and large offsets, where most of the anisotropy information is present. To overcome these problems, the reflectivity method (RM) was combined with linear (Luo et al., 2019; Huang et al., 2019) or nonlinear inversion schemes (Mallick and Adhikari, 2015; Li and Mallick, 2015; Padhi and Mallick, 2014). Although successful, these methods are difficult to use due to the complexity of the RM and extensive cost of the nonlinear optimization. Moreover, the inversion for

VTI media has more parameters (five or more) to be determined compared with the isotropic case, and local-minima solutions may easily. Recently, some studies attempted to reduce the number of parameters and proposed stepwise inversion strategies (Zhang et al., 2019a, 2019b). In addition, there are large sensitivity differences among the parameters, which leads to an unstable inversion. Furthermore, a joint multi-component inversion, compared to single PP-wave inversion, is helpful in reducing multiple solutions and improving the stability (Luo et al., 2018). This approach was applied successfully in isotropic AVO/AVA inversion (Auger et al., 2003; Veire and Landrø, 2006; Padhi and Mallick, 2013; Lu et al., 2015) and was also implemented in pre-stack inversion of anisotropic media (Grechka et al., 2002; Padhi and Mallick, 2014; Li and Mallick 2013, 2015; Lu et al., 2018).

A feasibility analysis is essential in multi-parameter inversion. Here, we compare a seismic-amplitude sensitivity analysis of commonly used parameters $\{V_P, V_S, \rho, \epsilon, \delta\}$ (P-wave velocity, S-wave velocity, bulk density, and Thomsen anisotropy parameters) to that of the stiffness set $\{c_{33}, c_{55}, c_{11}, c_{13}, \rho\}$. The comparison shows that stiffnesses c_{11} and c_{13} have apparently higher sensitivities to amplitudes than the Thomsen's parameters ϵ and δ , and the second set has a smaller sensitivity gap between the velocity- and anisotropy-related parameters, leading to a more stable and accurate inversion. Therefore, an indirect stable estimation scheme for anisotropy parameters of VTI media is proposed here: The stiffness set is inverted by pre-stack AVA inversion and then Thomsen anisotropy parameters are computed. In the first stage, the exact-Graebner-based prestack AVA inversion (EGI) is proposed, using the exact VTI Graebner (EG) equation as the forward engine to ensure a suitable modeling accuracy at medium and large offsets and overcome the weak-contrast limitation. Moreover, to save computation cost, a

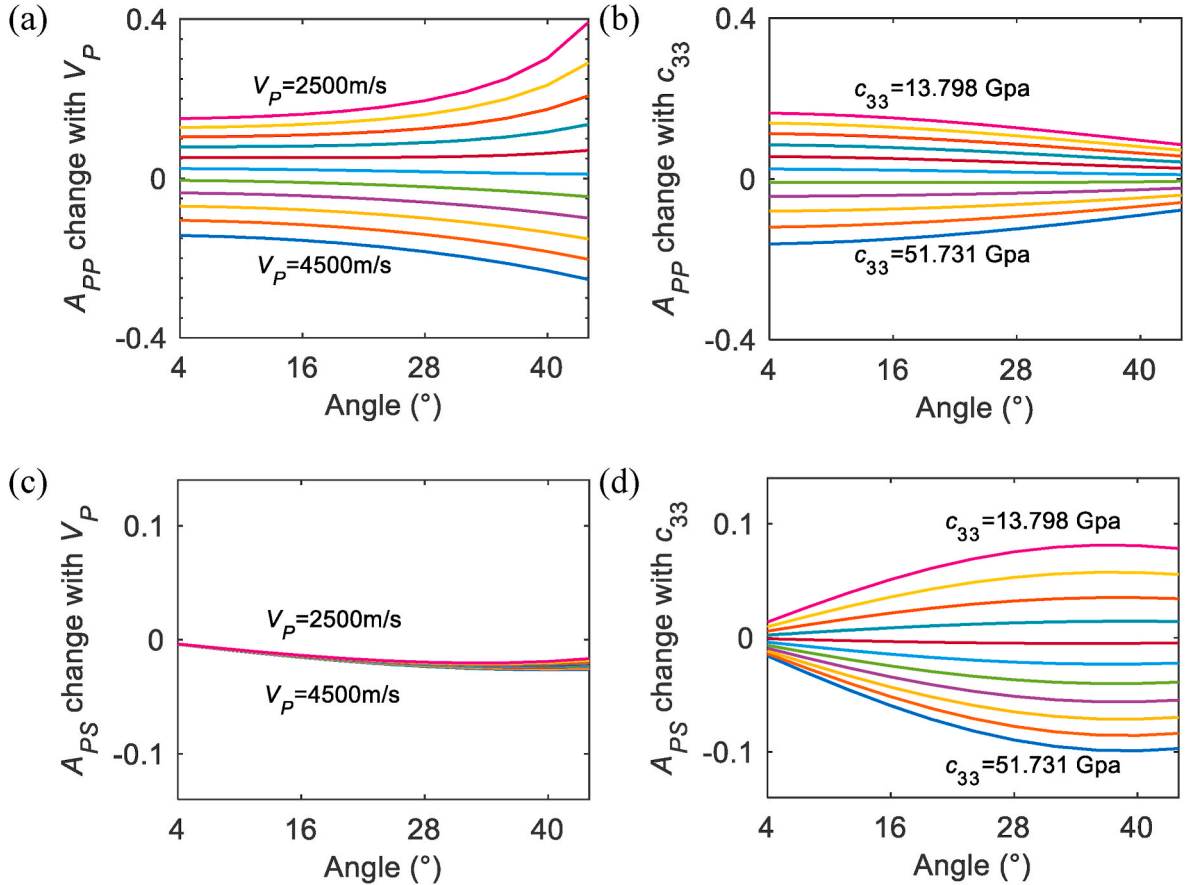


Fig. 1. Reflection amplitude of the PP- (A_{PP}) and PS-data (A_{PS}) as a function of the incidence angle. PP (a) and PS (c) amplitude variation with V_P , and PP (b) and PS (d) amplitude variation with c_{33} . The curves with different colors correspond to different V_P or c_{33} . (For interpretation of the references to color in this figure legend, the reader is referred to the Web version of this article.)

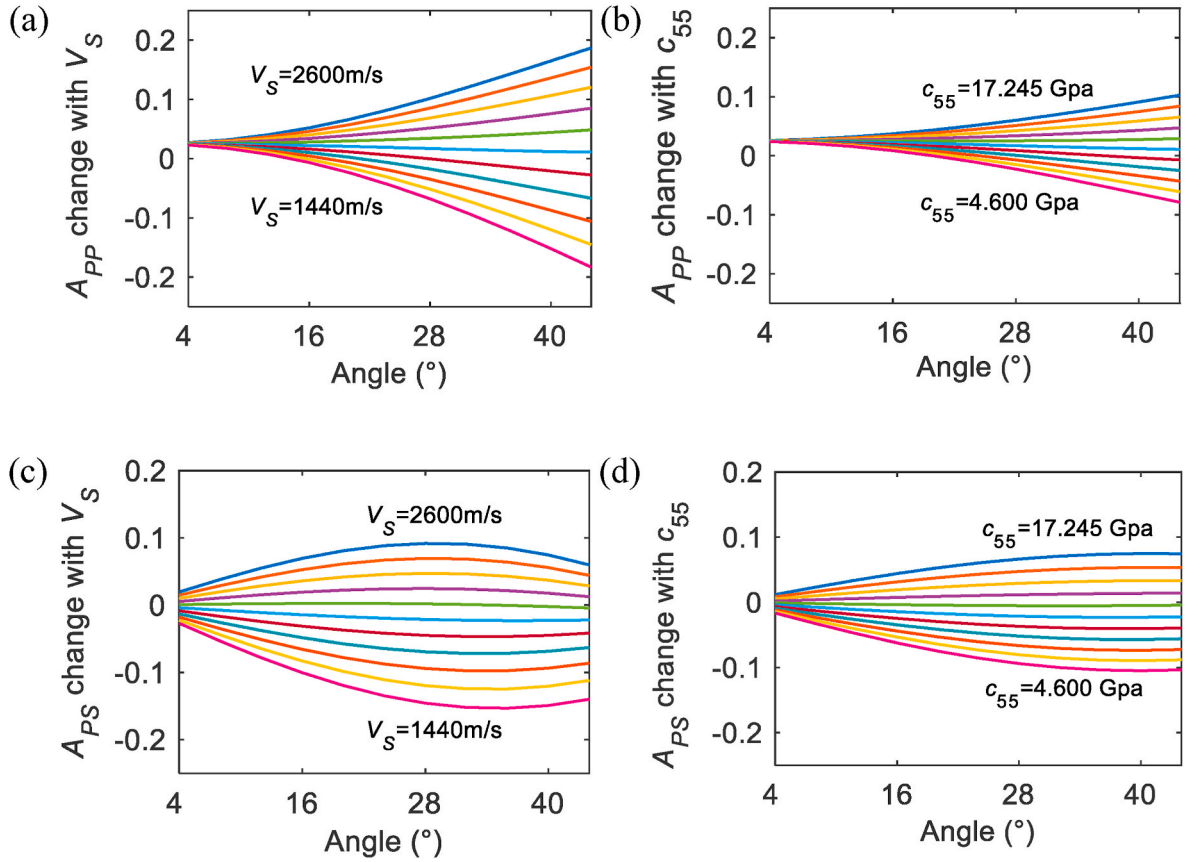


Fig. 2. Reflection amplitude of PP- (A_{PP}) and PS-data (A_{PS}) as a function of the incidence angle. PP (a) and PS (c) amplitude variation with V_S , and PP (b) and PS (d) amplitude variation with c_{55} . The curves with different colors correspond to different V_S or c_{55} . (For interpretation of the references to color in this figure legend, the reader is referred to the Web version of this article.)

linear inversion scheme is adopted. The Fréchet derivatives, the first-order derivatives of the EG modeling results with respect to the parameters, are the key factors of the method derived in this work. To speed up the convergence of the algorithm, the limited-memory Broyden-Fletcher-Goldfarb-Shanno (L-BFGS) method, adopting an iterative Newton method (Huang et al., 2019; Luo et al., 2019), is used to solve the objective function and compute an optimal solution. Adding PS waves to the PP-data inversion improves the algorithm, constituting the joint PP and PS exact-Graebner-based inversion (JEGI). We demonstrate the feasibility and effectiveness of the joint inversion method by using synthetic data of a borehole model and field multi-component seismic data.

2. Exact Graebner equation

Graebner (1992) gives the exact analytic expression of the RT coefficients for VTI media, which considers a plane wave incident on an interface separating two transversely-isotropic homogeneous media. The vector of the RT coefficients, corresponding to an incident P-wave, is

$$\mathbf{r} = [R_{PP} \ R_{PS} \ T_{PP} \ T_{PS}]^T. \quad (1)$$

where R_{PP} and R_{PS} are the reflection coefficients of the PP and PS waves, and T_{PP} and T_{PS} are the corresponding transmission coefficients. We have the solution

$$\mathbf{r} = \mathbf{S}^{-1} \cdot \mathbf{b} \quad (2)$$

where

$$\mathbf{S} = \begin{bmatrix} \ell_{1P} & n_{1S} & -\ell_{2P} & -n_{2S} \\ n_{1P} & -\ell_{1S} & n_{2P} & -\ell_{2S} \\ a_1 & b_1 & a_2 & b_2 \\ d_1 & e_1 & -d_2 & -e_2 \end{bmatrix}, \quad (3)$$

with

$$a_1 = (c_{55})_1 \cdot (s_{1P}\ell_{1P} + pn_{1P}), \quad b_1 = (c_{55})_1 \cdot (s_{1S}n_{1S} - p\ell_{1S}), \quad (4a)$$

$$a_2 = (c_{55})_2 \cdot (s_{2P}\ell_{2P} + pn_{2P}), \quad b_2 = (c_{55})_2 \cdot (s_{2S}n_{2S} - p\ell_{2S}), \quad (4b)$$

$$d_1 = p\ell_{1P}(c_{13})_1 + s_{1P}n_{1P}(c_{33})_1, \quad e_1 = pn_{1S}(c_{13})_1 - s_{1S}\ell_{1S}(c_{33})_1, \quad (4c)$$

$$-d_2 = -p\ell_{2P}(c_{13})_1 - s_{2P}n_{2P}(c_{33})_1, \quad -e_2 = -pn_{2S}(c_{13})_2 + s_{2S}\ell_{2S}(c_{33})_2. \quad (4d)$$

and

$$\mathbf{b} = [-\ell_{1P} \ n_{1P} \ (c_{55})_1 \cdot (s_{1P}\ell_{1P} + pn_{1P}) \quad -p\ell_{1P} \cdot (c_{13})_1 - s_{1P}n_{1P} \cdot (c_{33})_1]^T, \quad (5)$$

where the subscripts 1 and 2 represent the parameters of the upper and lower layers, respectively. The subscripts P and S refer to the P- and S-wave modes, respectively, s_v denotes the vertical slowness, where

$$s_P = \frac{1}{\sqrt{2}} \sqrt{K_1 - \sqrt{K_1^2 - 4K_2K_3}}, \quad (6a)$$

$$s_S = \frac{1}{\sqrt{2}} \sqrt{K_1 + \sqrt{K_1^2 - 4K_2K_3}}, \quad (6b)$$

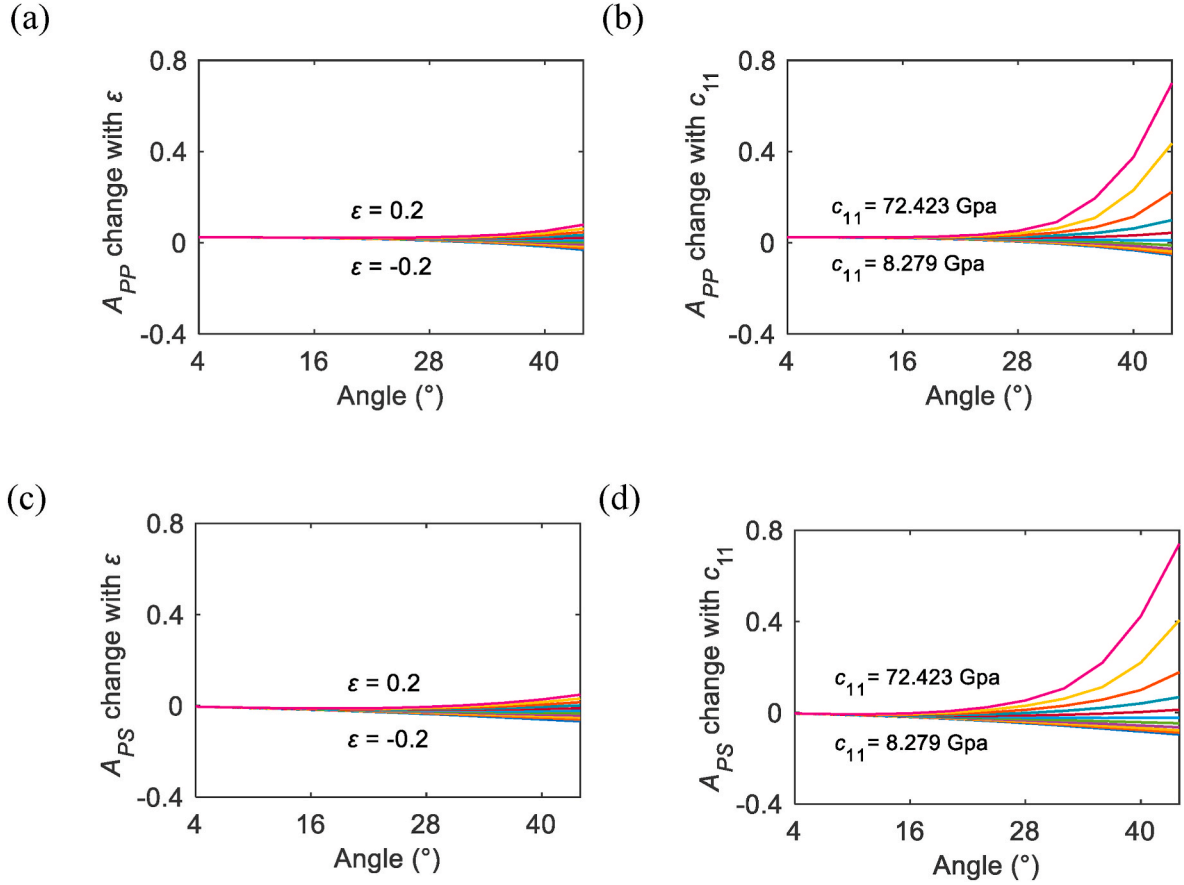


Fig. 3. Reflection amplitude of PP- (A_{PP}) and PS-data (A_{PS}) as a function of the incidence angle. PP (a) and PS (c) amplitude variation with ϵ , and PP (b) and PS (d) amplitude variation with c_{11} . The curves with different colors correspond to different ϵ or c_{11} . (For interpretation of the references to color in this figure legend, the reader is referred to the Web version of this article.)

where

$$K_1 = \frac{\rho}{c_{33}} + \frac{\rho}{c_{55}} - \left(\frac{c_{11}}{c_{55}} + \frac{c_{55}}{c_{33}} - \frac{(c_{11} + c_{55})^2}{c_{33}c_{55}} \right) \rho^2, \quad (7a)$$

$$K_2 = \frac{c_{11}}{c_{33}} \rho^2 - \frac{\rho}{c_{33}}, \quad K_3 = \rho^2 - \frac{\rho}{c_{55}} \quad (7b)$$

The symbols ℓ_p , n_p , ℓ_s and n_s in equations (3)–(5) are the direction cosine of the polarization vectors and the functions of elastic constants c_{11} , c_{13} , c_{33} and c_{55} and bulk density ρ

$$\ell_p = \sqrt{\frac{c_{33}s_p^2 + c_{55}p^2 - \rho}{c_{55}s_p^2 + c_{11}p^2 - \rho + c_{33}s_p^2 + c_{55}p^2 - \rho}}, \quad (8a)$$

$$n_p = \sqrt{\frac{c_{55}s_p^2 + c_{11}p^2 - \rho}{c_{55}s_p^2 + c_{11}p^2 - \rho + c_{33}s_p^2 + c_{55}p^2 - \rho}}, \quad (8b)$$

$$\ell_s = \sqrt{\frac{c_{55}s_s^2 + c_{11}p^2 - \rho}{c_{55}s_s^2 + c_{11}p^2 - \rho + c_{33}s_s^2 + c_{55}p^2 - \rho}}, \quad (8c)$$

$$n_s = \sqrt{\frac{c_{33}s_s^2 + c_{55}p^2 - \rho}{c_{55}s_s^2 + c_{11}p^2 - \rho + c_{33}s_s^2 + c_{55}p^2 - \rho}}. \quad (8d)$$

Thomsen (1986) introduced a new set of anisotropy coefficients for VTI media, including the vertical P-wave velocity V_p , vertical S-wave velocity V_s , bulk density ρ , and three dimensionless anisotropy parameters ϵ , δ and λ , which are related to the stiffnesses c_{ij} . According to Ruger

(2002), we can use V_s and γ to completely describe the SH-wave propagation. The P- and SV-wave propagation depend on V_p , V_s , ϵ and δ , which are related to the stiffnesses as

$$c_{33} = V_p^2 \rho, \quad c_{55} = V_s^2 \rho, \quad (9a)$$

$$c_{11} = (2\epsilon + 1)V_p^2 \rho = (2\epsilon + 1)c_{33} \quad (9b)$$

$$\begin{aligned} c_{13} &= \sqrt{2\delta V_p^2 \rho (V_p^2 \rho - V_s^2 \rho) + (V_p^2 \rho - V_s^2 \rho)^2} - \rho V_s^2 \\ &= \sqrt{2\delta c_{33} (c_{33} - c_{55}) + (c_{33} - c_{55})^2} - c_{55}. \end{aligned} \quad (9c)$$

3. Sensitivity analysis

In this section, we focus on the sensitivity analysis. In the standard inversion for VTI media, the commonly used parameter choice is $\{V_p, V_s, \rho, \epsilon, \delta\}$. Here, we consider another set consisting in c_{11} , c_{13} , c_{33} , c_{55} and ρ . According to equation (9), four parameter pairs include two velocity-related ones, V_p and c_{33} , V_s and c_{55} , and two anisotropy-related ones, ϵ and c_{11} , δ and c_{13} . From the modeling and inversion point of view, the sensitivity comparisons of these four parameter pairs are given.

3.1. AVA responses

The sensitivity is basically the AVA response variation with the parameters. A two-layer model (model 1) is set, whose base values are given in Table 1. We obtain several models by changing one parameter

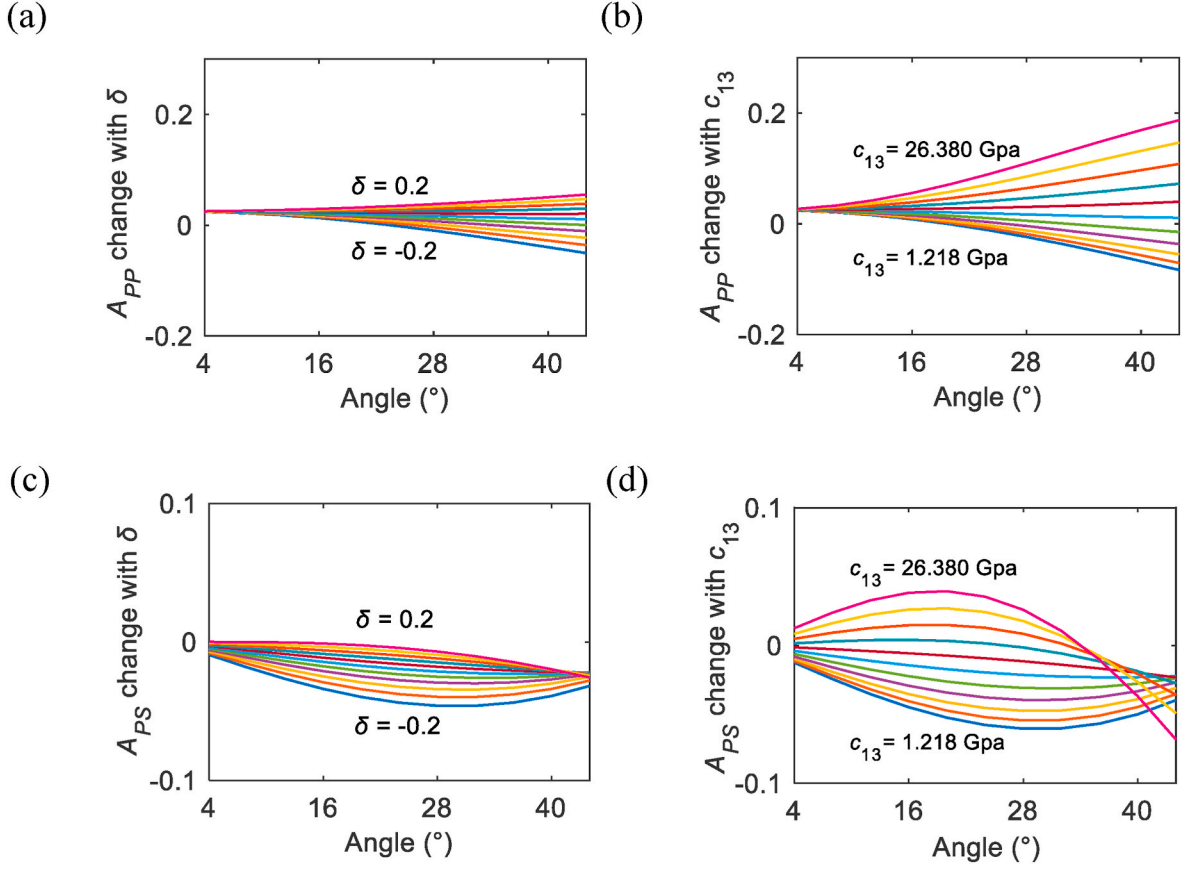


Fig. 4. Reflection amplitude of PP- (A_{PP}) and PS-data (A_{PS}) as a function of the incidence angle. PP (a) and PS (c) amplitude variation with δ , and PP (b) and PS (d) amplitude variation with c_{13} . The curves with different colors correspond to different δ or c_{13} . (For interpretation of the references to color in this figure legend, the reader is referred to the Web version of this article.)

Table 2
Model 2 properties. P-wave velocity, S-wave velocity, density, and anisotropy parameters.

Layer	V_P (m/s)	V_S (m/s)	ρ (g/cm ³)	ϵ	δ
Top	3400	1970	2.35	0.01	0.01
Bottom	3500	2020	2.40	0.0	0.0

of the lower layer with the other parameters fixed. The PP and PS synthetics are generated by convolving the EG reflection coefficients with a Ricker wavelet of 35 Hz dominant frequency. We extract the peak amplitudes along the interface and plot the PP-wave (A_{PP}) and PS-wave amplitudes (A_{PS}) variations (Figs. 1–4). Figures (a) and (b) show the AVA effects of the PP-wave and Figures (c) and (d) those of the PS-wave. It can be seen that the anisotropy-related parameters, including ϵ , δ , c_{11} and c_{13} , are sensitive only at medium and large offsets (angles) for both PP and PS seismic data, so that ensuring modeling accuracy within these ranges is essential to improve the inversion. Compared with approximations, the exact RT equation is therefore recommended for inversions. Besides, the velocity pairs (V_P and c_{33} , V_S and c_{55}) have higher sensitivity than the anisotropy parameter pairs (ϵ and c_{11} , δ and c_{13}), and compared with ϵ and δ , the stiffnesses c_{11} and c_{13} have higher amplitude sensitivities.

3.2. Posterior probability density

We take as the “true model” a homogeneous model with two elastic half spaces in contact. The input dataset of the inversion is the “observed data” \mathbf{D}^{obs} . Generally, the presence of noise leads to multiple solutions, i. e., the possible models. As the general solution of an inverse problem

consists of a probability over all possible models, we compute the posterior probabilities by using PP, and joint PP and PS data to test the sensitivity. Let \mathbf{m}_i represents one of the possible models and \mathbf{D}_i^{syn} the corresponding synthetic gather computed with the EG modeling. According to [Dębski and Tarantola \(1995\)](#), a posterior probability density can be derived as the product of a priori information $f(\mathbf{m})$ and a likelihood function $L(\mathbf{m})$,

$$g(\mathbf{m}) = const.f(\mathbf{m})L(\mathbf{m}), \quad (10)$$

where the likelihood function is used to measure the degree of fit between the synthetic data \mathbf{D}_{syn} and the observed data \mathbf{D}_{obs} ,

$$L(\mathbf{m}) = const.exp \left[-\frac{1}{2} \sum_i (\mathbf{D}^{obs} - \mathbf{D}_i^{syn})^2 / s \right]. \quad (11)$$

On the basis of [Dębski and Tarantola \(1995\)](#), we give the priori information expression of the two parameter sets. For $\{V_P, V_S, \rho, \epsilon, \delta\}$, the corresponding priori density is

$$f_{V_P V_S \rho \epsilon \delta}(V_P, V_S, \rho, \epsilon, \delta) = \frac{1}{\rho V_P V_S \left(\frac{3}{4} - \frac{V_S^2}{V_P^2} \right) (0.3 - \epsilon)(0.2 + \epsilon)(0.3 - \delta)(0.3 + \delta)} \quad (12)$$

where the singularities of this equation indicate the bounds imposed on the five parameters. First, V_P , V_S and ρ should be positive. Then, the two seismic velocities should satisfy the inequality constraint

$$V_P > \frac{2}{\sqrt{3}} V_S. \quad (13)$$

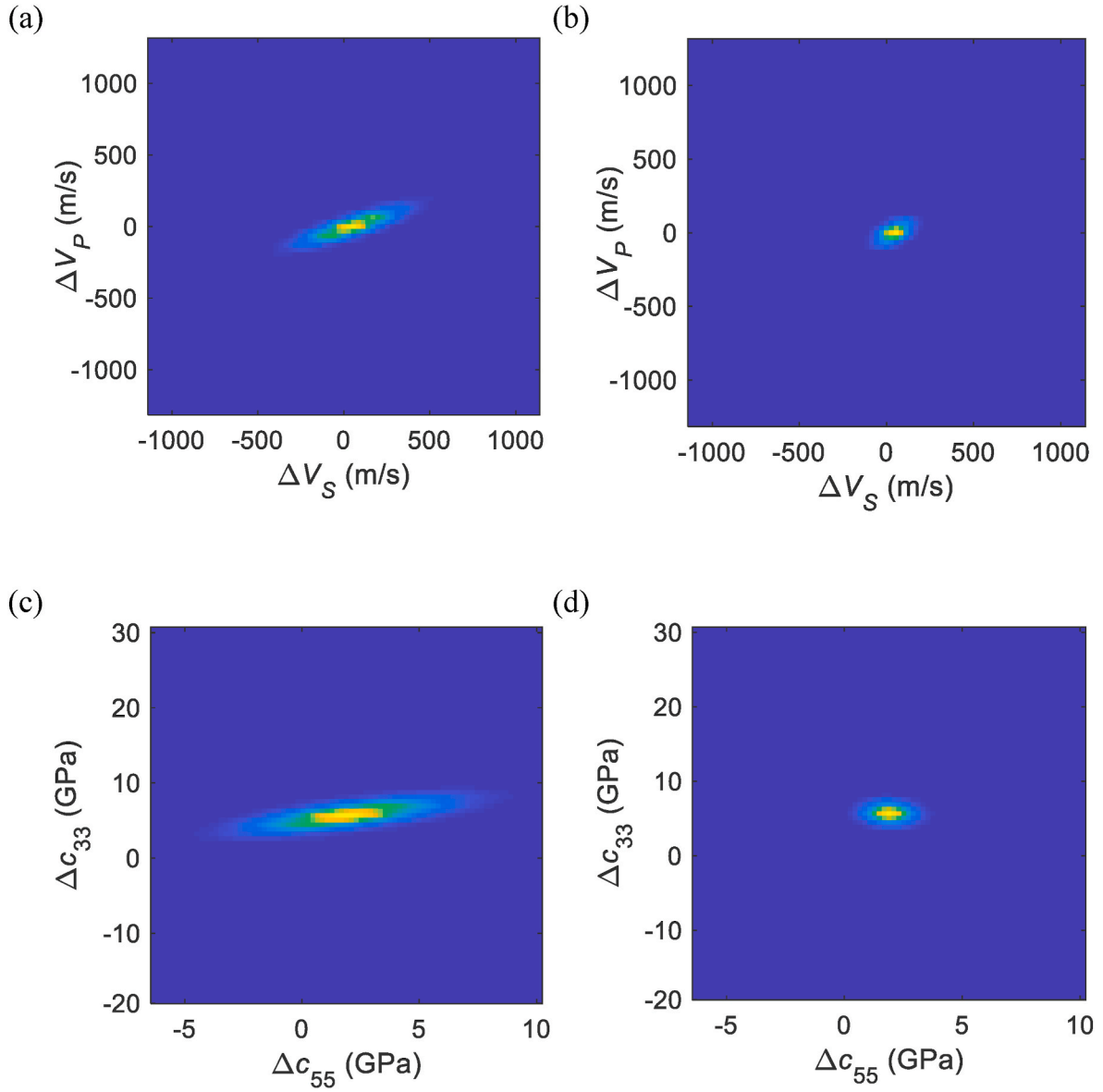


Fig. 5. 2D posterior probability densities of the velocity parameter pairs by using PP (a, c) and joint PP and PS data (b, d). (a, b) Densities of V_P and V_S , and (c, d) densities of c_{33} and c_{55} .

Based on the anisotropy results by [Thomsen \(1986\)](#), in most of the cases parameters ϵ and δ satisfy

$$-0.2 < \epsilon < 0.3, \quad -0.3 < \delta < 0.3. \quad (14)$$

The priori information for the set $\{c_{11}, c_{13}, c_{33}, c_{55}, \rho\}$ is

$$f_{c_{11}c_{13}c_{33}c_{55}\rho}(c_{11}, c_{13}, c_{33}, c_{55}, \rho) = \frac{1}{c_{11}c_{13}c_{33}c_{55}\rho \left(\frac{3}{4} - \frac{c_{33}}{c_{55}} \right)} \quad (15)$$

According to equation (9), the stiffnesses c_{11} , c_{13} , c_{33} and c_{55} should be greater than zero. The relationship between the two velocities in equation (13) imposes

$$\frac{c_{55}}{c_{33}} < \frac{3}{4}. \quad (16)$$

The ‘‘true model’’ (model 2) is given in [Table 2](#). V_P , V_S , ϵ and δ of the lower layer vary in the ranges of -1300 m/s to 1300 m/s, -1260 m/s to

1260 m/s, -0.265 g/cm³ to 0.195 g/cm³, -0.2 to 0.2 and -0.2 to 0.2 , respectively. The second parameter set has the corresponding ranges $c_{33} = -19$ to 30.4 GPa, $c_{55} = -8.1$ to 15 GPa, $c_{11} = -23.2$ to 51 GPa and $c_{13} = -53$ to 84.2 GPa. The probability density describing the posterior information can be computed with equation (10). [Figs. 5 and 6](#) show the 2D probability density of the pairs (V_P and c_{33} , V_S and c_{55}) and (ϵ and c_{11} , δ and c_{13}), by using the PP ([a](#) and [c](#)) and joint PP and PS data ([b](#) and [d](#)). [Fig. 5a](#) and [b](#) represent the 2D probabilities of V_P and V_S , [Fig. 5c](#) and [d](#) shows those of c_{33} and c_{55} , [Fig. 6a](#) and [b](#) those of ϵ and δ , and [Fig. 6c](#) and [d](#) those of c_{11} and c_{13} . More focused probability density means more seismic sensitivity. Compared with the anisotropy pairs ([Fig. 6](#)), the velocity pairs show higher sensitivity ([Fig. 5](#)). The comparison of the two sets shows that the sensitivities of c_{33} and c_{55} ([Fig. 5c](#) and [d](#)) are slightly lower than those of V_P and V_S ([Fig. 5a](#) and [b](#)). However, there is a significant improvement of the sensitivities of c_{11} and c_{13} ([Fig. 6c](#) and [d](#)) compared with those of ϵ and δ ([Fig. 6a](#) and [b](#)). The conclusions we obtain here are similar to those of the previous section, which tells the

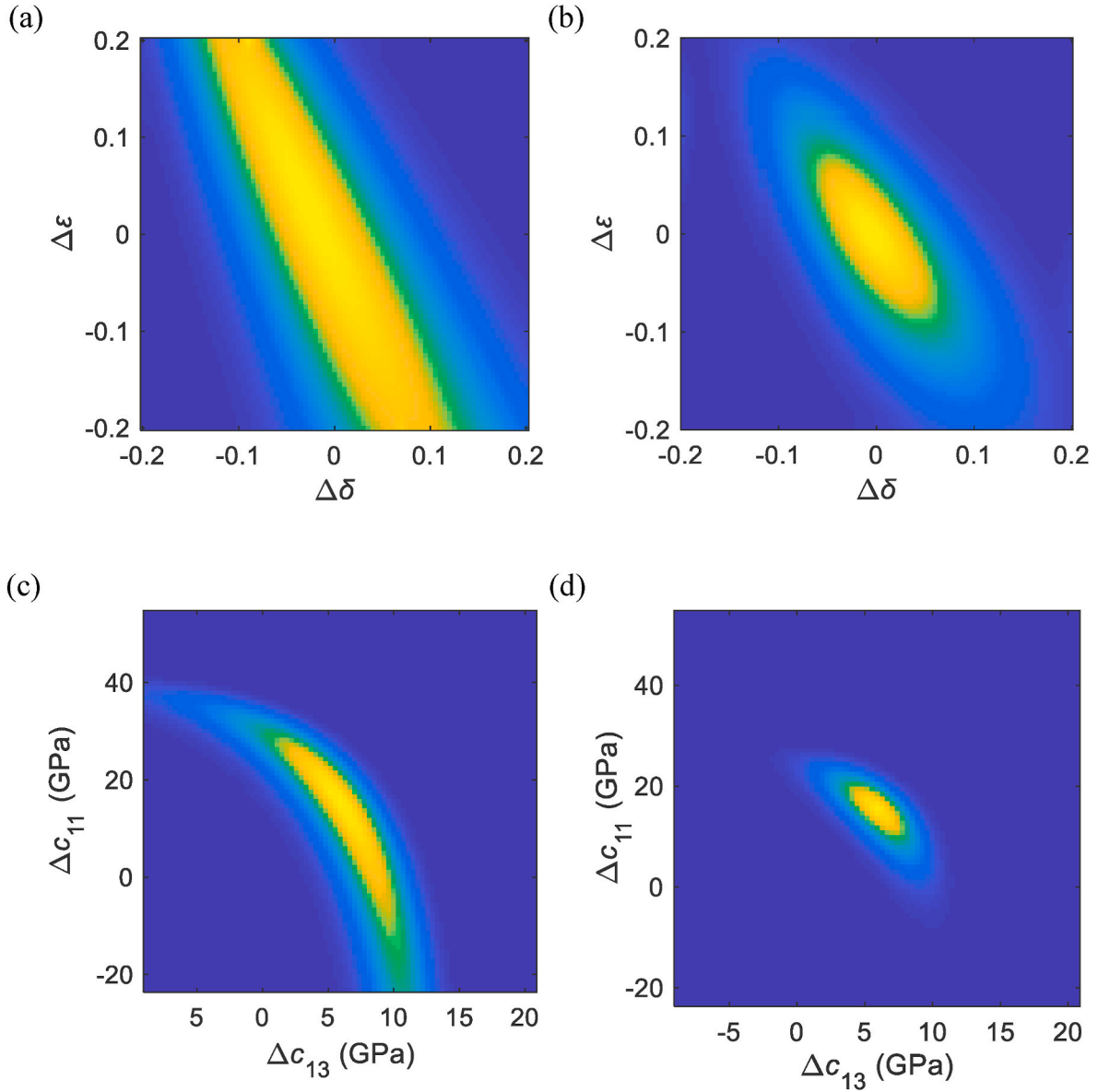


Fig. 6. 2D posterior probability densities of the anisotropy parameter pairs by using PP (a, c) and joint PP and PS data (b, d). (a, b) Densities of ϵ and δ , and (c, d) densities of c_{11} and c_{13} .

stiffness parameter set has a smaller sensitivity gap between velocity- and anisotropy-related parameters. It is notable because, theoretically, smaller sensitivity gaps enhance the accuracy and stability of a multi-parameter inversion. Moreover, the joint records result in a better convergence of the probability density than the PP data, which can be better seen from Figures b and d. Although the sensitivities of ϵ and δ are improved by using the PP and PS records, it is not sensitive enough.

4. Anisotropic AVA inversion

The set $\{V_P, V_S, \rho, \epsilon, \delta\}$ has higher sensitivity gap between velocity- and anisotropy-related parameters leading to more inversion instability. Here, we use the exact Graebner equation, the set $\{c_{33}, c_{55}, c_{11}, c_{13}, \rho\}$, and the joint PP and PS inversion scheme to obtain better estimates.

4.1. Inversion with the graebner equation

Let F be the forward modeling equation,

$$F(\mathbf{d}, \mathbf{m}) = \mathbf{d} - G(\mathbf{m}) = 0 \quad (17)$$

where the symbol $G(\mathbf{m})$ represents the forward engine, where is a nonlinear function of the model parameters \mathbf{m} . In multi-parameter inversion of VTI media, vector \mathbf{m} is

$$\mathbf{m} = [(c_{11})_1, \dots, (c_{11})_M, (c_{13})_1, \dots, (c_{13})_M, (c_{33})_1, \dots, (c_{33})_M, (c_{55})_1, \dots, (c_{55})_M, \rho_1, \dots, \rho_M] \quad (18)$$

In the linear inversion scheme, a cost (objective) function is set up and solved by an optimization method. However, the inversion problem is generally ill-posed. A regularization is adopted and a weight parameter λ is introduced to balance the contributions of data misfit and model constraints. Then, the objective function is

$$S(\mathbf{m}) = (1 - \alpha) \cdot [\mathbf{d}_{PS} - G_{PS}(\mathbf{m})]^T [\mathbf{d}_{PS} - G_{PS}(\mathbf{m})] + \alpha [\mathbf{d}_{PP} - G_{PP}(\mathbf{m})]^T [\mathbf{d}_{PP} - G_{PP}(\mathbf{m})] + \lambda (\mathbf{m} - \mathbf{u})^T \mathbf{C}_m^{-1} (\mathbf{m} - \mathbf{u}) \quad (19)$$

where \mathbf{d}_{PP} and \mathbf{d}_{PS} are the real PP and PS data sets, $G_{PP}(\mathbf{m})$ and $G_{PS}(\mathbf{m})$ represent the synthetic PP and PS gathers. The joint penta-variable Gaussian distribution is used as the constraint condition. \mathbf{u} is the expectation of \mathbf{m} . Since the elastic parameters of subsurface rocks show

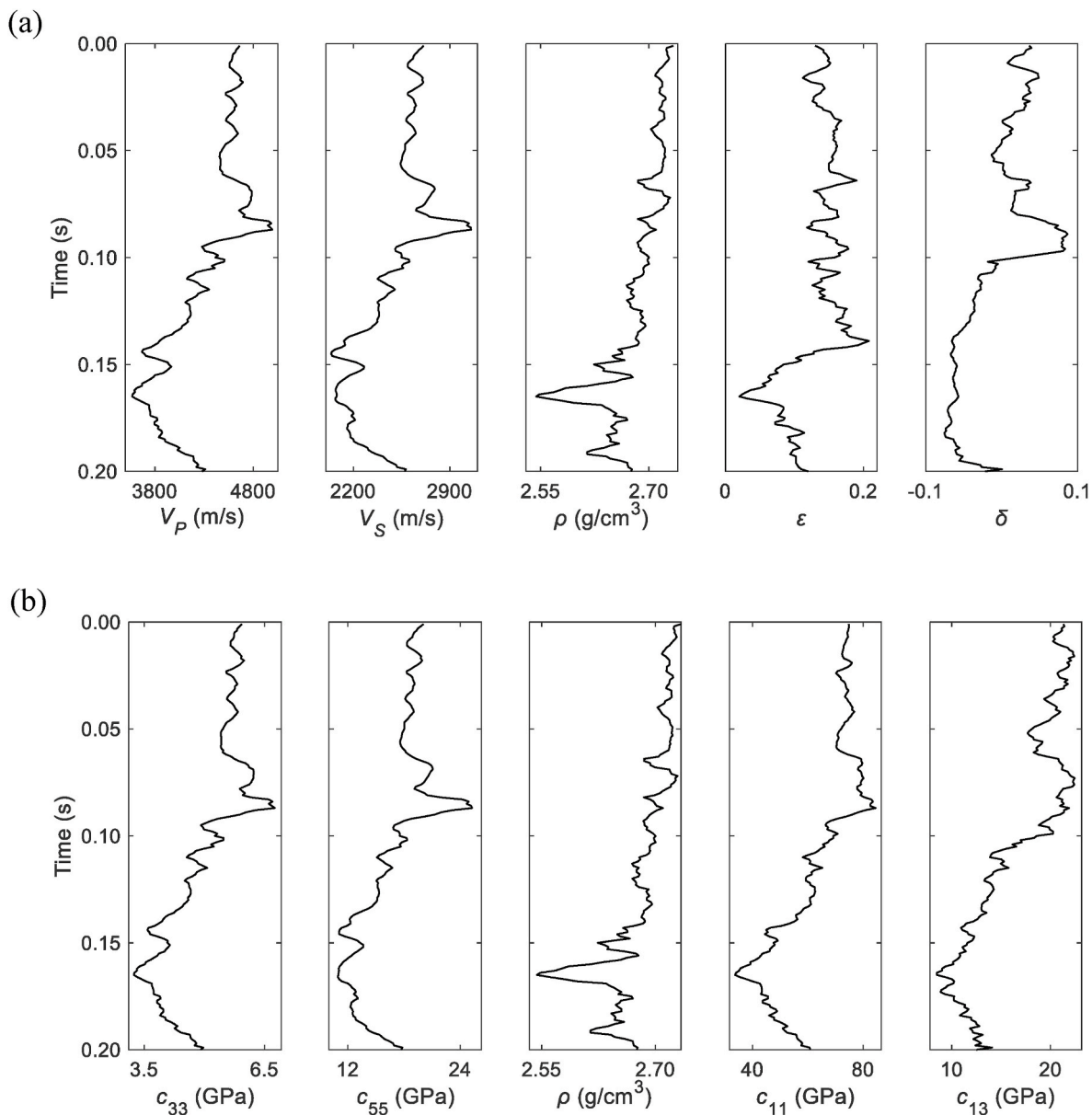


Fig. 7. Well logs for the synthetic data test after Backus averaging and corresponding stiffness profiles. (a) First parameter choice, from left to right the panels are V_p , V_s , ρ , ϵ and δ . (b) Second parameter choice computed by using the first set in Figure (a); from left to right the panels are c_{33} , c_{55} , ρ , c_{11} and c_{13} .

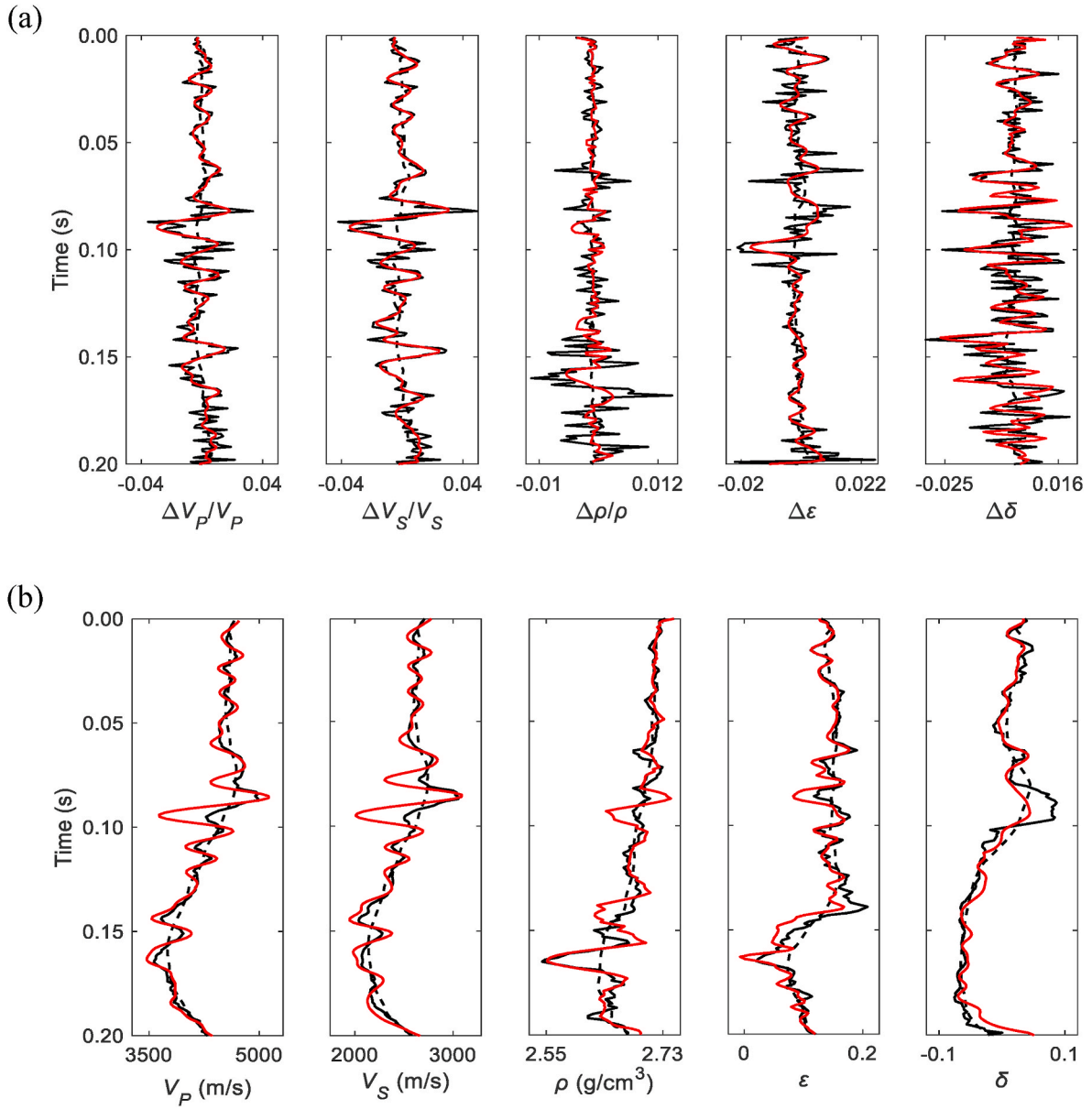


Fig. 8. Results of the Rüger-approximation-based AVA inversion by using joint PP and PS data. (a) Inverted reflectivities, including $\Delta V_p/V_p$, $\Delta V_s/V_s$, $\Delta \rho/\rho$, $\Delta \epsilon$ and $\Delta \delta$. (b) Converted target parameters by using the reflectivities, including the V_p , V_s , ρ , ϵ and δ results. The red solid, black solid and black dotted lines represent the inversion results, true logs and initial models, respectively. (For interpretation of the references to color in this figure legend, the reader is referred to the Web version of this article.)

Table 3

Root-mean-square error (RMSE) and correlation coefficient (CC) between the inversion results and the true models of the test well by using JRAI.

Inverted parameter	V_p	V_s	ρ	ϵ	δ
RMSE	4.3386	5.9793	1.6236	10.2109	17.9363
CC	0.9832	0.9748	0.9266	0.9687	0.9602

strong statistical correlations, C_m , the covariance matrix of the parameter vector with $5M \times 5M$ dimension, is introduced to improve the stability of multi-parameter inversion. It can be expressed as

$$C_m = \begin{bmatrix} \sigma_{c_{11}c_{11}} & \sigma_{c_{11}c_{13}} & \sigma_{c_{11}c_{33}} & \sigma_{c_{11}c_{55}} & \sigma_{c_{11}\rho} \\ \sigma_{c_{11}c_{13}} & \sigma_{c_{13}c_{13}} & \sigma_{c_{13}c_{33}} & \sigma_{c_{13}c_{55}} & \sigma_{c_{11}c_{11}} \\ \sigma_{c_{11}c_{33}} & \sigma_{c_{13}c_{33}} & \sigma_{c_{33}c_{33}} & \sigma_{c_{33}c_{55}} & \sigma_{c_{33}c_{55}} \\ \sigma_{c_{11}c_{55}} & \sigma_{c_{13}c_{55}} & \sigma_{c_{33}c_{55}} & \sigma_{c_{55}c_{55}} & \sigma_{c_{55}\rho} \\ \sigma_{c_{11}\rho} & \sigma_{c_{13}\rho} & \sigma_{c_{33}\rho} & \sigma_{c_{55}\rho} & \sigma_{\rho\rho} \end{bmatrix}_{5M \times 5M} \quad (20a)$$

where σ is a $M \times M$ dimension matrix. Taking $\sigma_{c_{11}c_{11}}$ as an example, which has the form as

$$\sigma_{c_{11}c_{11}} = \begin{bmatrix} \sigma_{(c_{11})_1(c_{11})_1} & \cdots & 0 \\ \vdots & \ddots & \vdots \\ 0 & \cdots & \sigma_{(c_{11})_M(c_{11})_M} \end{bmatrix}. \quad (20b)$$

By introducing the L-BFGS algorithm, i.e., an optimization method with a good convergence rate and the acceptable storage requirement, the iteration is expressed as

$$\mathbf{m}_{k+1} = \mathbf{m}_k - \kappa_k H(\mathbf{m}_k)^{-1} \cdot J(\mathbf{m}_k) \quad (21)$$

where \mathbf{m}_k is the result of the k th iteration, κ_k denotes the step size of the k th iteration, obtained by the strong Wolfe line search algorithm (Zhi et al., 2016), $J(\mathbf{m})$ represents the Jacobian matrix, the first-order derivative of the objective function as

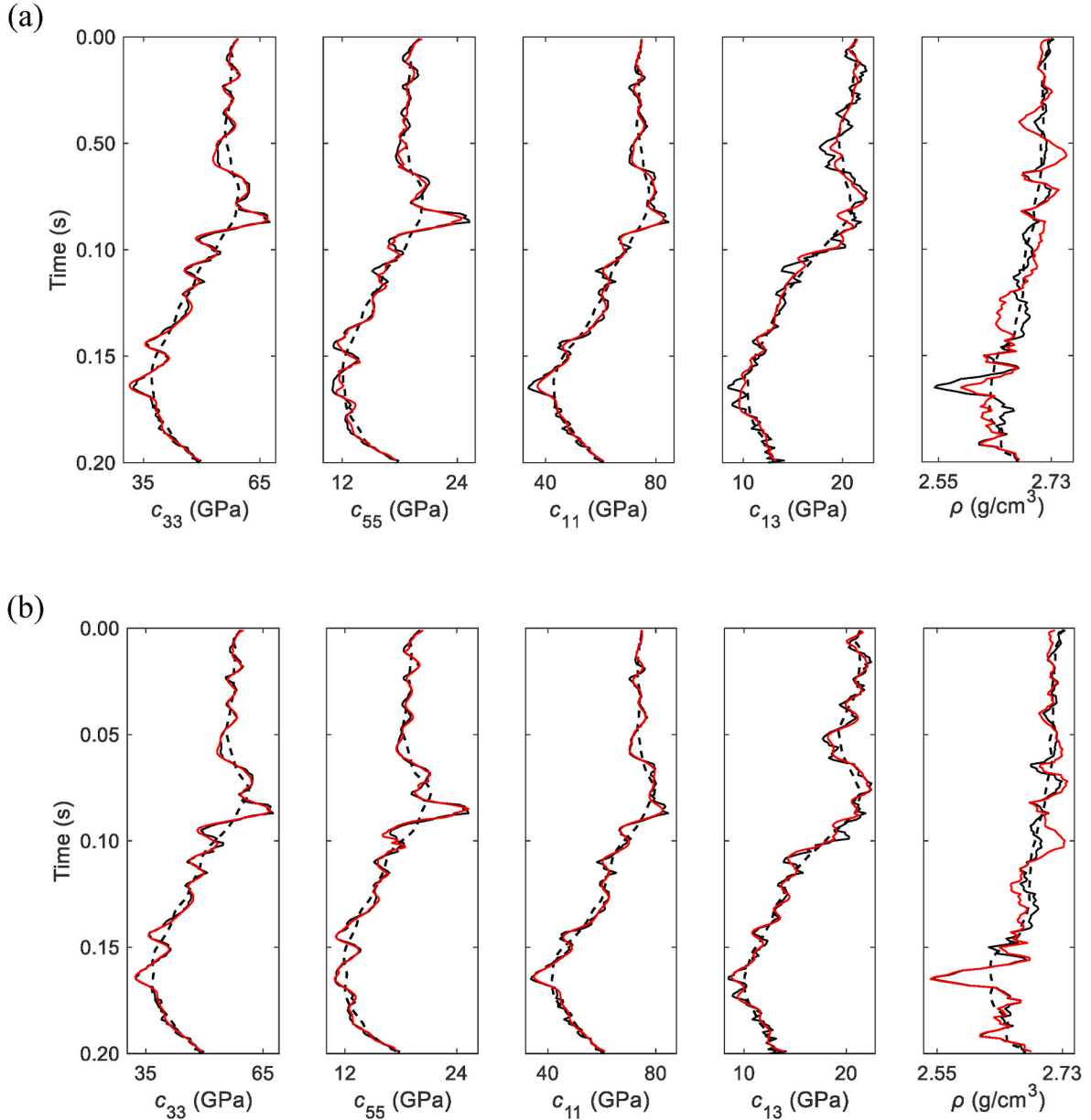


Fig. 9. Inversion results of the Exact-Graebner-based AVA inversion by using PP data (a) and joint PP and PS data (b), including the c_{33} , c_{55} , c_{11} , c_{13} and ρ results. The red solid, black solid and black dotted lines represent the inversion results, true logs and initial models, respectively. (For interpretation of the references to color in this figure legend, the reader is referred to the Web version of this article.)

$$J(\mathbf{m}) = \nabla_{\mathbf{m}} S(\mathbf{m}) = \alpha \left[\frac{\partial G_{PP}(\mathbf{m})}{\partial \mathbf{m}} \right]^T [\mathbf{d}_{PP} - G_{PP}(\mathbf{m})] \quad (22)$$

$$+ (1 - \alpha) \left[\frac{\partial G_{PS}(\mathbf{m})}{\partial \mathbf{m}} \right]^T [\mathbf{d}_{PS} - G_{PS}(\mathbf{m})] + \lambda C_m^{-1} (\mathbf{m} - \mathbf{u})$$

and $H(\mathbf{m})$ denotes the pseudo Hessian matrix of the objective function and is computed by an iterative algorithm. For the first iteration, we set

$$H_1(\mathbf{m})^{-1} = \left[(1 - \alpha) \cdot \left[\frac{\partial G_{PS}(\mathbf{m})}{\partial \mathbf{m}} \right]^T \frac{\partial G_{PS}(\mathbf{m})}{\partial \mathbf{m}} \right] \quad (23)$$

$$\alpha \left[\frac{\partial G_{PP}(\mathbf{m})}{\partial \mathbf{m}} \right]^T \frac{\partial G_{PP}(\mathbf{m})}{\partial \mathbf{m}} + \lambda C_m^{-1} \right]^{-1}$$

where $\frac{\partial G_{PP}(\mathbf{m})}{\partial \mathbf{m}}$ and $\frac{\partial G_{PS}(\mathbf{m})}{\partial \mathbf{m}}$ are the Fréchet-derivative matrices, the partial derivatives of the PP and PS forward engines with respect to the model parameters. For $j \geq 2$, according to the L-BFGS algorithm, the Hessian

matrix can be computed as

$$H_{i+1}(\mathbf{m})^{-1} = \mathbf{V}_i^T H_i(\mathbf{m})^{-1} \mathbf{V}_i + \mathbf{K}_i \cdot (\mathbf{m}_i - \mathbf{m}_{i-1}) \cdot (\mathbf{m}_i - \mathbf{m}_{i-1})^T, \quad (24a)$$

with

$$\mathbf{V}_i = \mathbf{I} - \mathbf{K}_i \cdot [J_i(\mathbf{m}) - J_{i-1}(\mathbf{m})] \cdot (\mathbf{m}_i - \mathbf{m}_{i-1})^T \quad (24b)$$

and

$$\mathbf{K}_i = \frac{1}{[J_i(\mathbf{m}) - J_{i-1}(\mathbf{m})]^T (\mathbf{m}_i - \mathbf{m}_{i-1})}, \quad (24c)$$

where \mathbf{I} denotes the identity matrix.

4.2. Fréchet derivatives

The Fréchet derivatives, the partial derivatives of the PP and PS forward operator, can be obtained as

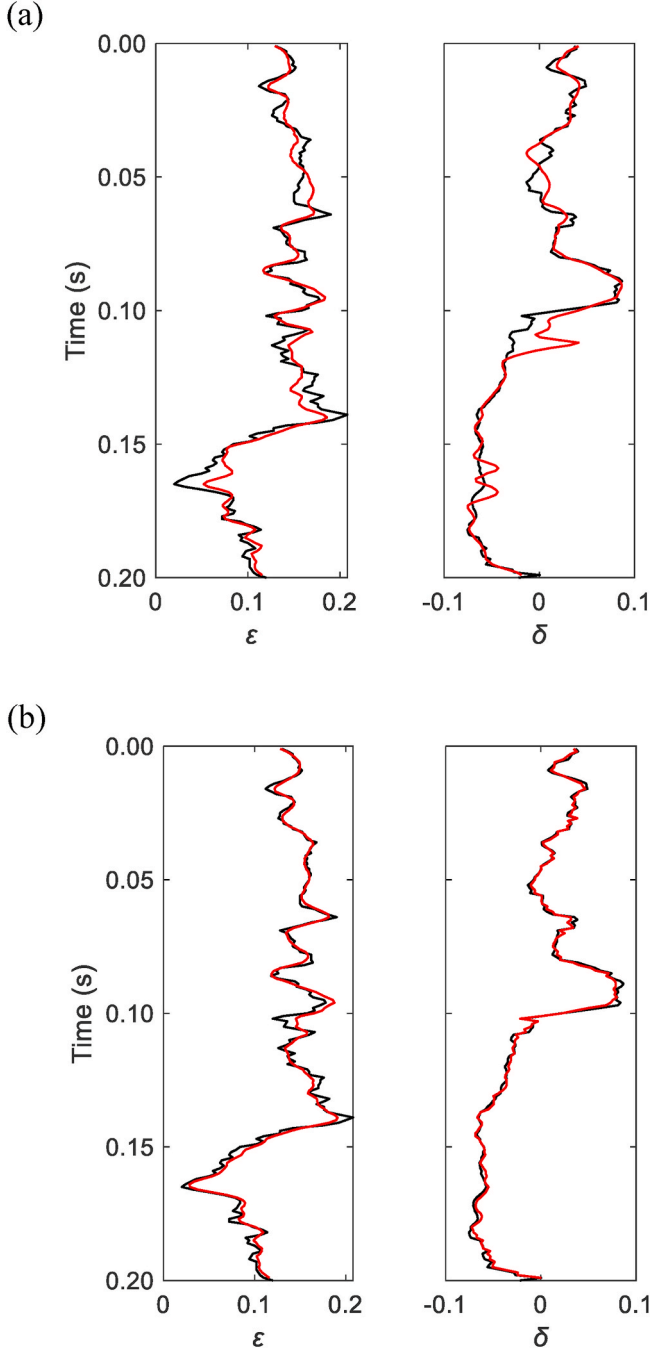


Fig. 10. Computed anisotropy curves by using the inversion results of Fig. 9, including ϵ and δ . (a) Anisotropy parameter estimations by using the PP data, and (b) estimations by using the joint PP and PS data. The red and black solid lines represent the inversion results and true logs, respectively. (For interpretation of the references to color in this figure legend, the reader is referred to the Web version of this article.)

Table 4

RMSE and CC between the inversion results and the true models of the test well by using EGI and JEGI.

Inversion results		c_{33}	c_{55}	c_{11}	c_{13}	ρ
EGI	RMSE	1.3119	2.3276	2.6553	3.8023	1.3164
	CC	0.9962	0.9924	0.9911	0.9829	0.8525
JEGI	RMSE	1.0980	1.2863	1.6729	1.9920	0.8368
	CC	0.9984	0.9974	0.9951	0.9943	0.9539

Table 5

RMSE and CC between the computed anisotropy parameters and the true models of the test well by using EGI and JEGI.

Inversion results		ϵ	δ
EGI	RMSE	7.1054	10.5308
	CC	0.9887	0.9805
JEGI	RMSE	3.3682	7.2439
	CC	0.9934	0.9923

$$\frac{\partial \mathbf{G}_{PP}(\mathbf{m})}{\partial \mathbf{m}} = \mathbf{W}_{PP} \frac{\partial \mathbf{r}_{PP}(\mathbf{m})}{\partial \mathbf{m}}, \quad \frac{\partial \mathbf{G}_{PS}(\mathbf{m})}{\partial \mathbf{m}} = \mathbf{W}_{PS} \frac{\partial \mathbf{r}_{PS}(\mathbf{m})}{\partial \mathbf{m}}, \quad (25)$$

where \mathbf{W}_{PP} and \mathbf{W}_{PS} are the wavelet matrices of PP and PS synthetics, respectively, and $\mathbf{r}_{PP}(\mathbf{m})$ and $\mathbf{r}_{PS}(\mathbf{m})$ correspond to the reflection-coefficient sequences of the PP and PS waves, respectively. Moreover,

$$\frac{\partial \mathbf{r}}{\partial \mathbf{m}} = \begin{bmatrix} \frac{\partial \mathbf{r}(\theta_1)}{\partial c_{11}} & \frac{\partial \mathbf{r}(\theta_1)}{\partial c_{13}} & \frac{\partial \mathbf{r}(\theta_1)}{\partial c_{33}} & \frac{\partial \mathbf{r}(\theta_1)}{\partial c_{55}} & \frac{\partial \mathbf{r}(\theta_1)}{\partial \rho} \\ \vdots & \vdots & \vdots & \vdots & \vdots \\ \frac{\partial \mathbf{r}(\theta_K)}{\partial c_{11}} & \frac{\partial \mathbf{r}(\theta_K)}{\partial c_{13}} & \frac{\partial \mathbf{r}(\theta_K)}{\partial c_{33}} & \frac{\partial \mathbf{r}(\theta_K)}{\partial c_{55}} & \frac{\partial \mathbf{r}(\theta_K)}{\partial \rho} \end{bmatrix}, \quad (26)$$

where $\frac{\partial \mathbf{r}(\theta_i)}{\partial \mathbf{m}}$ denotes the partial-derivative matrix corresponding to the incidence angle θ_i with $i = 1, 2, \dots, K$. If c_{11} is considered as an example, we have

$$\frac{\partial \mathbf{r}(\theta_i)}{\partial c_{11}} = \begin{bmatrix} \frac{\partial \mathbf{r}(\theta_i, t_1)}{\partial (c_{11})^1} & \frac{\partial \mathbf{r}(\theta_i, t_1)}{\partial (c_{11})^2} & 0 & \dots & \dots & 0 \\ 0 & \frac{\partial \mathbf{r}(\theta_i, t_2)}{\partial (c_{11})^2} & \frac{\partial \mathbf{r}(\theta_i, t_2)}{\partial (c_{11})^3} & 0 & \vdots & \vdots \\ \vdots & 0 & 0 & \ddots & 0 & 0 \\ \vdots & \vdots & \vdots & 0 & \frac{\partial \mathbf{r}(\theta_i, t_{M-1})}{\partial (c_{11})^{M-1}} & \frac{\partial \mathbf{r}(\theta_i, t_{M-1})}{\partial (c_{11})^M} \\ 0 & \dots & \dots & \dots & 0 & \frac{\partial \mathbf{r}(\theta_i, t_M)}{\partial (c_{11})^M} \end{bmatrix}_{M \times M} \quad (27)$$

where $\mathbf{c}_{11} = [(c_{11})^1 (c_{11})^2 \dots (c_{11})^M]^T$ is a $M \times 1$ vector.

To obtain the derivatives of the reflection coefficients defined by the exact Graebner equation, we first consider

$$\mathbf{m} = [(c_{11})_1, (c_{11})_2, (c_{13})_1, (c_{13})_2, (c_{33})_1, (c_{33})_2, (c_{55})_1, (c_{55})_2, \rho_1, \rho_2]^T. \quad (28)$$

The subscripts 1 and 2 represent the parameters of top and bottom layers across an interface. Then, the partial derivatives with respect to \mathbf{m}^* are computed on both sides of equation (2) to obtain

$$\frac{\partial \mathbf{r}}{\partial \mathbf{m}^*} = \mathbf{S}^{-1} \frac{\partial \mathbf{b}}{\partial \mathbf{m}^*} - \mathbf{S}^{-1} \frac{\partial \mathbf{S}}{\partial \mathbf{m}^*} \mathbf{r} \quad (29)$$

for each variable of the vector \mathbf{m} . The partial-derivative equations can be expressed as

$$\frac{\partial \mathbf{r}}{\partial (c_{11})_1} = \mathbf{S}^{-1} \frac{\partial \mathbf{b}}{\partial (c_{11})_1} - \mathbf{S}^{-1} \frac{\partial \mathbf{S}}{\partial (c_{11})_1} \mathbf{r}, \quad (30)$$

$$\frac{\partial \mathbf{r}}{\partial (c_{11})_2} = -\mathbf{S}^{-1} \frac{\partial \mathbf{S}}{\partial (c_{11})_2} \mathbf{r}, \quad (31)$$

$$\frac{\partial \mathbf{r}}{\partial (c_{13})_1} = \mathbf{S}^{-1} \frac{\partial \mathbf{b}}{\partial (c_{13})_1} - \mathbf{S}^{-1} \frac{\partial \mathbf{S}}{\partial (c_{13})_1} \mathbf{r}, \quad (32)$$

$$\frac{\partial \mathbf{r}}{\partial (c_{13})_2} = -\mathbf{S}^{-1} \frac{\partial \mathbf{S}}{\partial (c_{13})_2} \mathbf{r}, \quad (33)$$

$$\frac{\partial \mathbf{r}}{\partial (c_{33})_1} = \mathbf{S}^{-1} \frac{\partial \mathbf{b}}{\partial (c_{33})_1} - \mathbf{S}^{-1} \frac{\partial \mathbf{S}}{\partial (c_{33})_1} \mathbf{r}, \quad (34)$$

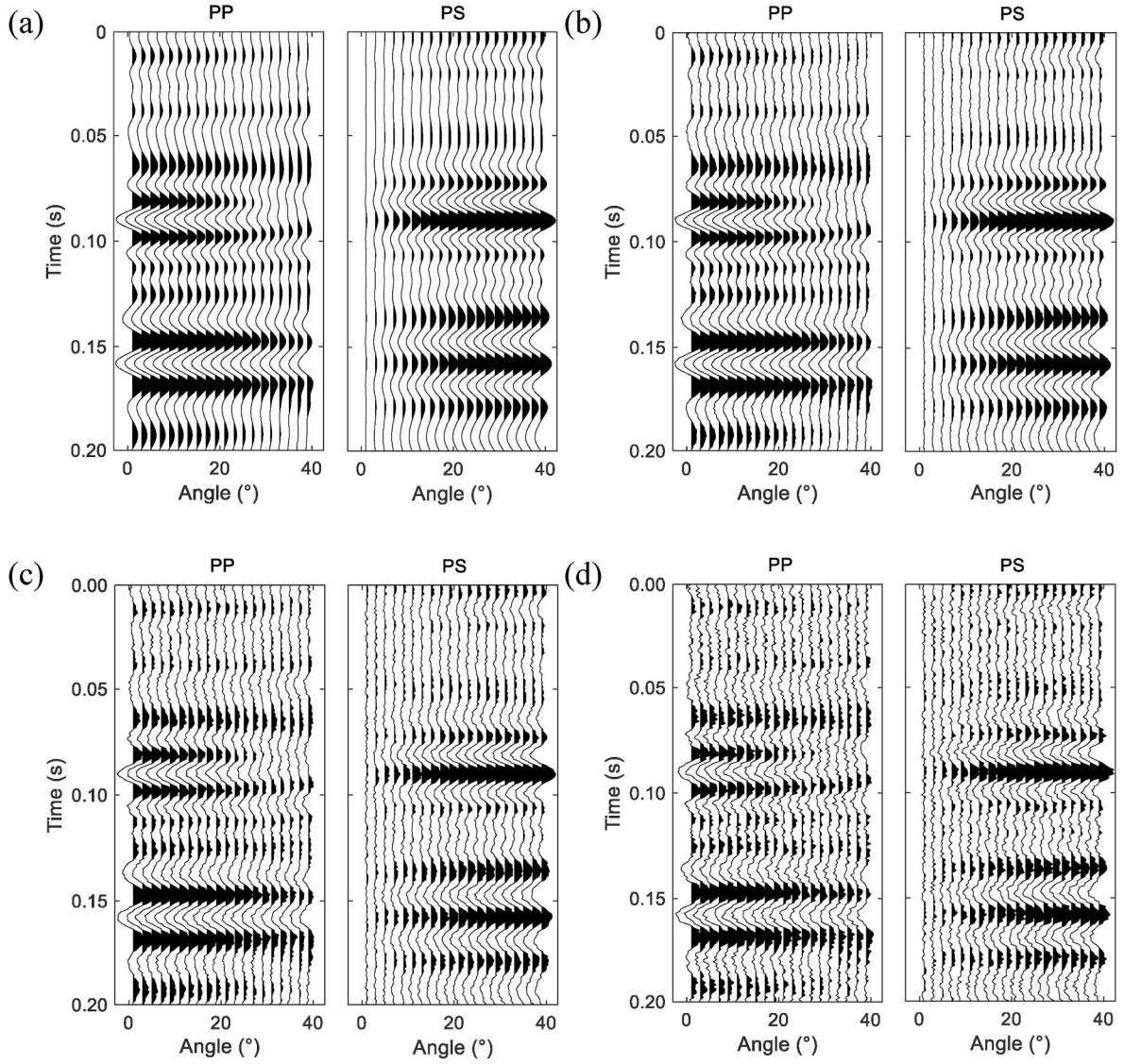


Fig. 11. Synthetic PP (left panels) and PS seismograms (right panels) in the PP time domain computed with the EG with different SNR, (a) SNR = ∞ , (b) SNR = 10, (c) SNR = 5, and (d) SNR = 3.

$$\frac{\partial \mathbf{r}}{\partial (c_{33})_2} = -\mathbf{S}^{-1} \frac{\partial \mathbf{S}}{\partial (c_{33})_2} \mathbf{r}, \quad (35)$$

$$\frac{\partial \mathbf{r}}{\partial (c_{55})_1} = \mathbf{S}^{-1} \frac{\partial \mathbf{b}}{\partial (c_{55})_1} - \mathbf{S}^{-1} \frac{\partial \mathbf{S}}{\partial (c_{55})_1} \mathbf{r}, \quad (36)$$

$$\frac{\partial \mathbf{r}}{\partial (c_{55})_2} = -\mathbf{S}^{-1} \frac{\partial \mathbf{S}}{\partial (c_{55})_2} \mathbf{r}, \quad (37)$$

$$\frac{\partial \mathbf{r}}{\partial \rho_1} = \mathbf{S}^{-1} \frac{\partial \mathbf{b}}{\partial \rho_1} - \mathbf{S}^{-1} \frac{\partial \mathbf{S}}{\partial \rho_1} \mathbf{r}, \quad (38)$$

$$\frac{\partial \mathbf{r}}{\partial \rho_2} = -\mathbf{S}^{-1} \frac{\partial \mathbf{S}}{\partial \rho_2} \mathbf{r}. \quad (39)$$

The key problem is to compute the partial derivatives of the intermediate matrices \mathbf{S} and \mathbf{b} with respect to the variables of the model vector \mathbf{m} in equation (22), including $\frac{\partial \mathbf{S}}{\partial (c_{11})_1}$, $\frac{\partial \mathbf{S}}{\partial (c_{11})_2}$, $\frac{\partial \mathbf{S}}{\partial (c_{13})_1}$, $\frac{\partial \mathbf{S}}{\partial (c_{13})_2}$, $\frac{\partial \mathbf{S}}{\partial (c_{33})_1}$, $\frac{\partial \mathbf{S}}{\partial (c_{33})_2}$, $\frac{\partial \mathbf{S}}{\partial (c_{55})_1}$, $\frac{\partial \mathbf{S}}{\partial (c_{55})_2}$, $\frac{\partial \mathbf{b}}{\partial \rho_1}$, $\frac{\partial \mathbf{b}}{\partial \rho_2}$, $\frac{\partial \mathbf{b}}{\partial (c_{11})_1}$, $\frac{\partial \mathbf{b}}{\partial (c_{13})_1}$, $\frac{\partial \mathbf{b}}{\partial (c_{33})_1}$, $\frac{\partial \mathbf{b}}{\partial (c_{55})_1}$, $\frac{\partial \mathbf{b}}{\partial \rho_1}$. The specific expressions are given in the Appendix.

5. Inversion analysis

5.1. Numerical synthetic data

A well-log model is used to test the proposed method with synthetic data. The target parameters of the EG-based inversion are c_{33} , c_{55} , c_{11} , c_{13} and ρ , and the corresponding models (see Fig. 7b) are computed with the curves of Fig. 7a. The input synthetic PP and PS data are subcritical, with angles ranging from 1 to 40°, and generated with a convolution of the reflection coefficients from the EG modeling and the Ricker wavelet with dominant frequencies of 40 Hz for the PP-wave, and 30 Hz for the PS-wave. The synthetic example neglects multiples, converted waves and noise. Three inversion methods are tested in this section, including the joint PP and PS Rüger-approximation-based direct inversion (JRAI), the single PP data exact-Graebner-based two-step inversion (EGI), and the joint PP and PS exact-Graebner-based two-step inversion (JEGI).

The prestack inversion based on the approximate equation computes the reflectivities first and then converts them into target parameters by using a trace integral algorithm. Fig. 8 shows the inverted reflectivities, $\frac{\Delta V_p}{V_p}$, $\frac{\Delta V_s}{V_s}$, $\frac{\Delta \rho}{\rho}$, $\Delta \epsilon$ and $\Delta \delta$ of the JRAI (Fig. 8a) and the corresponding inversion results of five parameters corrected by the low frequency

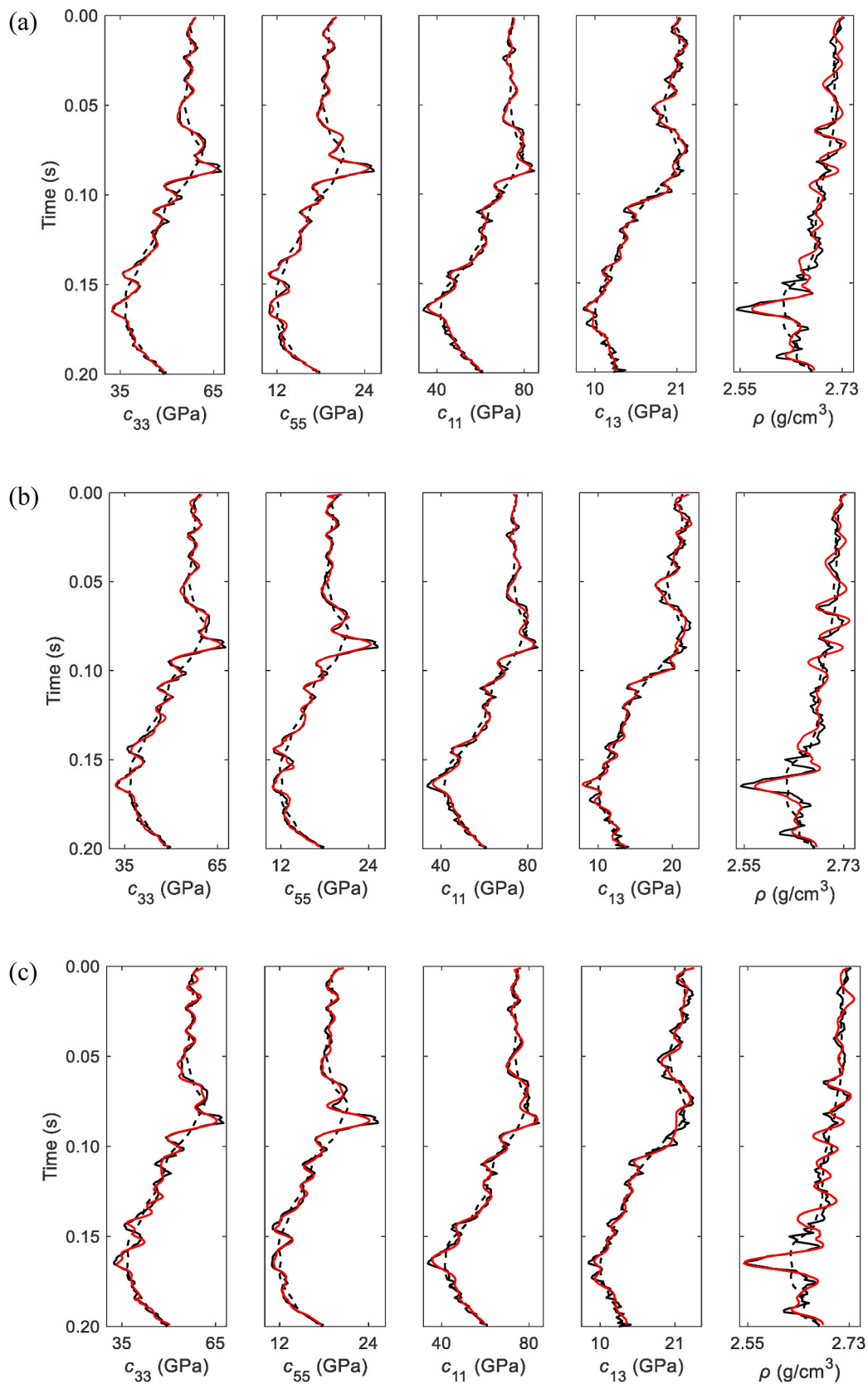


Fig. 12. The inversion results of JEGI algorithm by using the noisy angle gathers of Fig. 11. (a) SNR = 10 (Fig. 11a). (b) SNR = 5 (Fig. 11b). (c) SNR = 3 (Fig. 11c). The initial, true and inverted curves are given by the black dotted, blue solid and red solid lines, respectively. (For interpretation of the references to color in this figure legend, the reader is referred to the Web version of this article.)

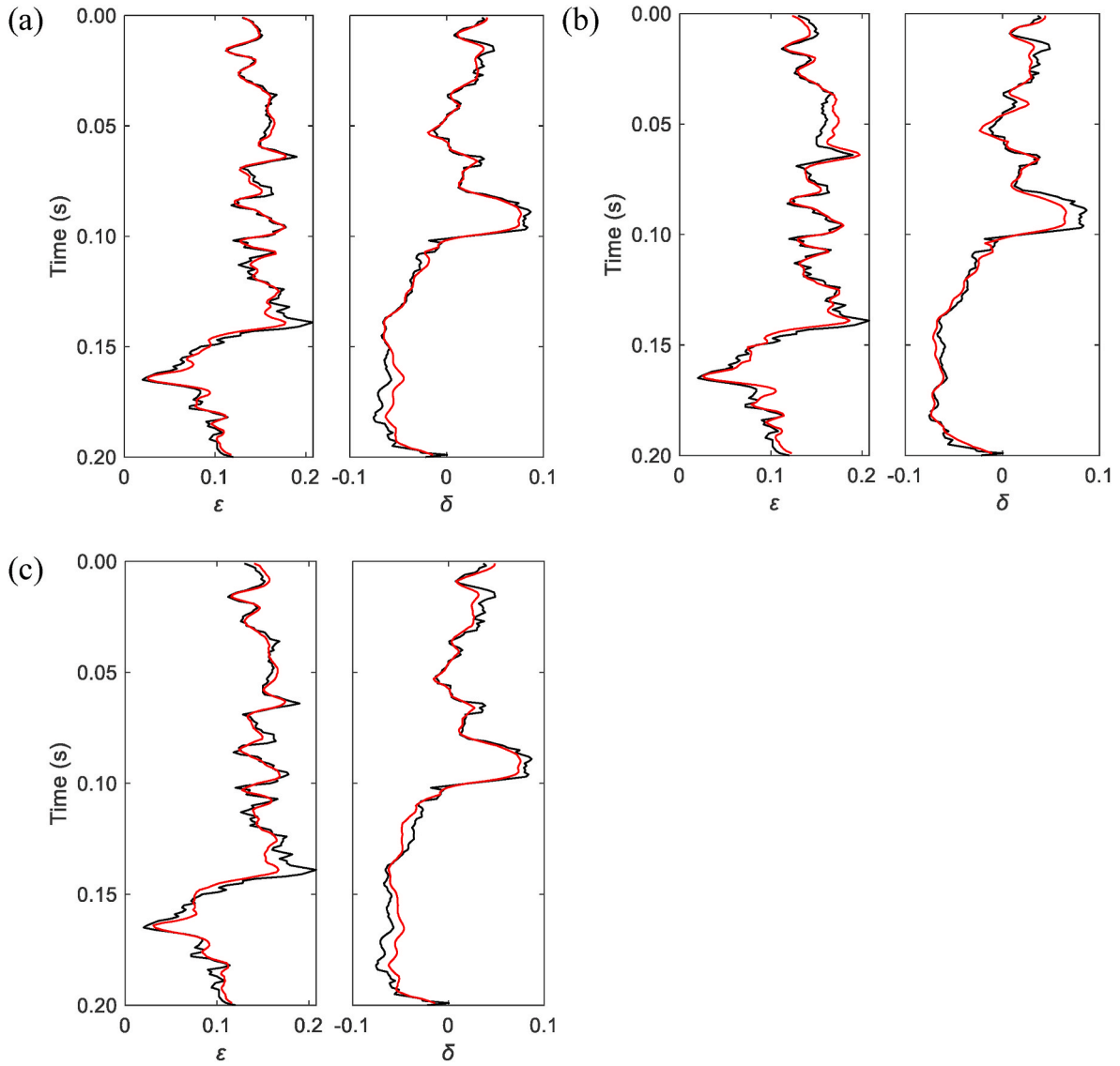


Fig. 13. Computed anisotropy curves by using the inversion results of Fig. 9, including ϵ and δ . Anisotropy parameter estimations are given by using the noisy gathers with (a) SNR = 10, (b) SNR = 5, and (c) SNR = 3, respectively. The red and black solid lines represent the inversion results and true logs, respectively. (For interpretation of the references to color in this figure legend, the reader is referred to the Web version of this article.)

initial models (Fig. 8b). The Rüger-approximation-based inversion, even using the joint PP and PS data, does not yield acceptable reflectivities. Moreover, the trace integral method computes the parameters layer by layer and degrades the estimation of the target parameters, mainly for deep sections. The poor estimation of the anisotropy parameters ϵ and δ is reflected in the low root-mean-square-errors (RMSEs) and correlation coefficients (CCs) between the true models and the inverted results of the JRAI. The RMSE of the JRAI are shown in Table 3: 4.3386 (V_p), 5.9793 (V_s), 1.6236 (ρ), 10.2109 (ϵ), and 17.9363 (δ). The CC are

0.9832 (V_p), 0.9748 (V_s), 0.9266 (ρ), 0.9687 (ϵ), and 0.9602 (δ).

Fig. 9 shows the results of the first step of the EGI (a) and JEGI (b), including the stiffness and density, and Fig. 10 shows the computed anisotropy parameters ϵ and δ of the EGI (a) and JEGI (b) by using the results of Fig. 9a and b. EGI yields acceptable results for c_{33} , c_{55} and c_{11} with CCs: 0.9962, 0.9924, and 0.9911, respectively, and RMSEs: 1.3119, 2.3276, 2.6553, but unsatisfactory results for c_{13} and ρ with CCs: 0.9829, 0.8525 and RMSEs: 3.8023, 1.3164. Therefore, the estimation of δ by EGI has poor CC (0.9805) and RMSE (10.5308) due to the low accuracy

Table 6

RMSE and CC between the inversion results with different noise levels and the true models of the test well by using JEGI.

JEGI results		c_{33}	c_{55}	c_{11}	c_{13}	ρ
SNR = 10	RMSE	1.3161	1.6451	1.7788	2.3247	0.9011
	CC	0.9978	0.9970	0.9967	0.9958	0.9466
SNR = 5	RMSE	1.5805	1.8677	2.0747	2.6767	1.0154
	CC	0.9965	0.9958	0.9945	0.9928	0.9307
SNR = 3	RMSE	1.8997	1.9500	2.2647	3.0835	1.2044
	CC	0.9945	0.9937	0.9920	0.9889	0.9202

Table 7

RMSE and CC between the computed anisotropy parameters corresponding to different noise levels and the true models of the test well by using JEGI.

JEGI results		ϵ	δ
SNR = 10	RMSE	5.2972	11.8522
	CC	0.9881	0.9795
SNR = 5	RMSE	6.6424	14.4015
	CC	0.9712	0.9510
SNR = 3	RMSE	7.3917	17.7942
	CC	0.9695	0.9387

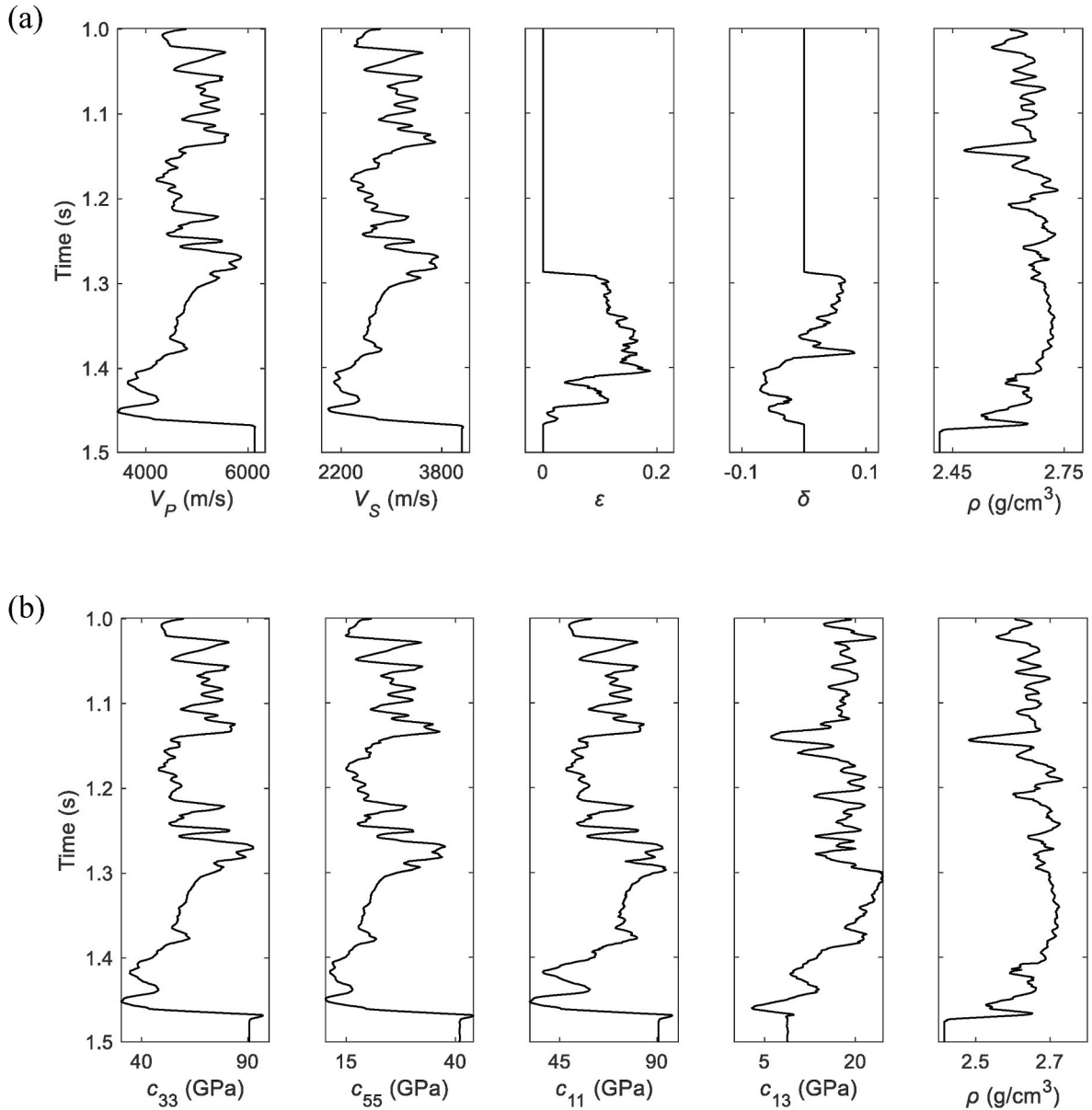


Fig. 14. Well logs at CDP 400. (a) Logs of the P-wave velocity, S-wave velocity, anisotropy parameters ϵ , anisotropy parameters δ and density. (b) Computed profiles of the stiffnesses c_{33} , c_{55} , c_{11} , c_{13} and density.

in the estimation of c_{13} . For JEGI, the CCs of the five parameters are: 0.9984 (c_{33}), 0.9974 (c_{55}), 0.9951 (c_{11}), 0.9943 (c_{13}) and 0.9539 (ρ) and the RMSEs are: 1.0980 (c_{33}), 1.4863 (c_{55}), 1.6729 (c_{11}), 1.9920 (c_{13}) and 0.8368 (ρ). All the RMSEs and CCs are shown in Table 4. Compared with EGI, the stiffness c_{13} is significantly improved by JEGI, which yields better results of the anisotropy parameter δ with CC: 0.9923 and RMSE: 7.2439, displayed in Table 5. The RMSE for density is the smallest as compared with the other parameters, and the reason may be that the relative change of density is smaller than the others.

In both, EGI and JEGI, the inverted stiffnesses c_{33} , c_{55} , c_{11} and c_{13} are closer to the true model than the inverted density, because the stiffnesses are of the same order of magnitude and much larger than the density (see equation (9)). Although the large gap in order of magnitude between the density and the stiffnesses leads to poor density results, according to equation (9), the computed anisotropy parameters are unaffected. The bulk density is important for lithology and fluid identification, but this work is focused on a robust method for anisotropy parameter inversion.

5.2. Noise effect analysis

The noise effect on the accuracy of the proposed JEGI method is investigated. The Gaussian random noise is added to the synthetic gathers (Fig. 11a) to obtain the new input gathers, as shown in Fig. 11b, c and d, which correspond to the noisy gathers with SNR (the ratio of the root-mean-square amplitude of the signal to that of the noise) of 10, 5 and 3, respectively. Fig. 12a–c shows the first step inversion results of JEGI by using input gathers with SNR = 10, 5 and 3, respectively. The correspondingly computed anisotropy parameters ϵ and δ from the second step are shown in Fig. 13. The RMSEs and CCs of the inverted stiffness coefficients and the computed anisotropy parameters are shown in Tables 6 and 7, respectively.

Fig. 12c, the corresponding inversion results for the noisy gathers with SNR = 3, shows that the quality of c_{33} , c_{55} and c_{11} are still acceptable because the CCs reach 0.9945 (c_{33}), 0.9937 (c_{55}) and 0.9920 (c_{11}). However, the inverted c_{13} is unsatisfactory with RMSE (3.0835) and CC (0.9889). Given the data with a high noise level (SNR = 3), due to the effect of c_{13} , the estimation of δ has relatively poor RMSE

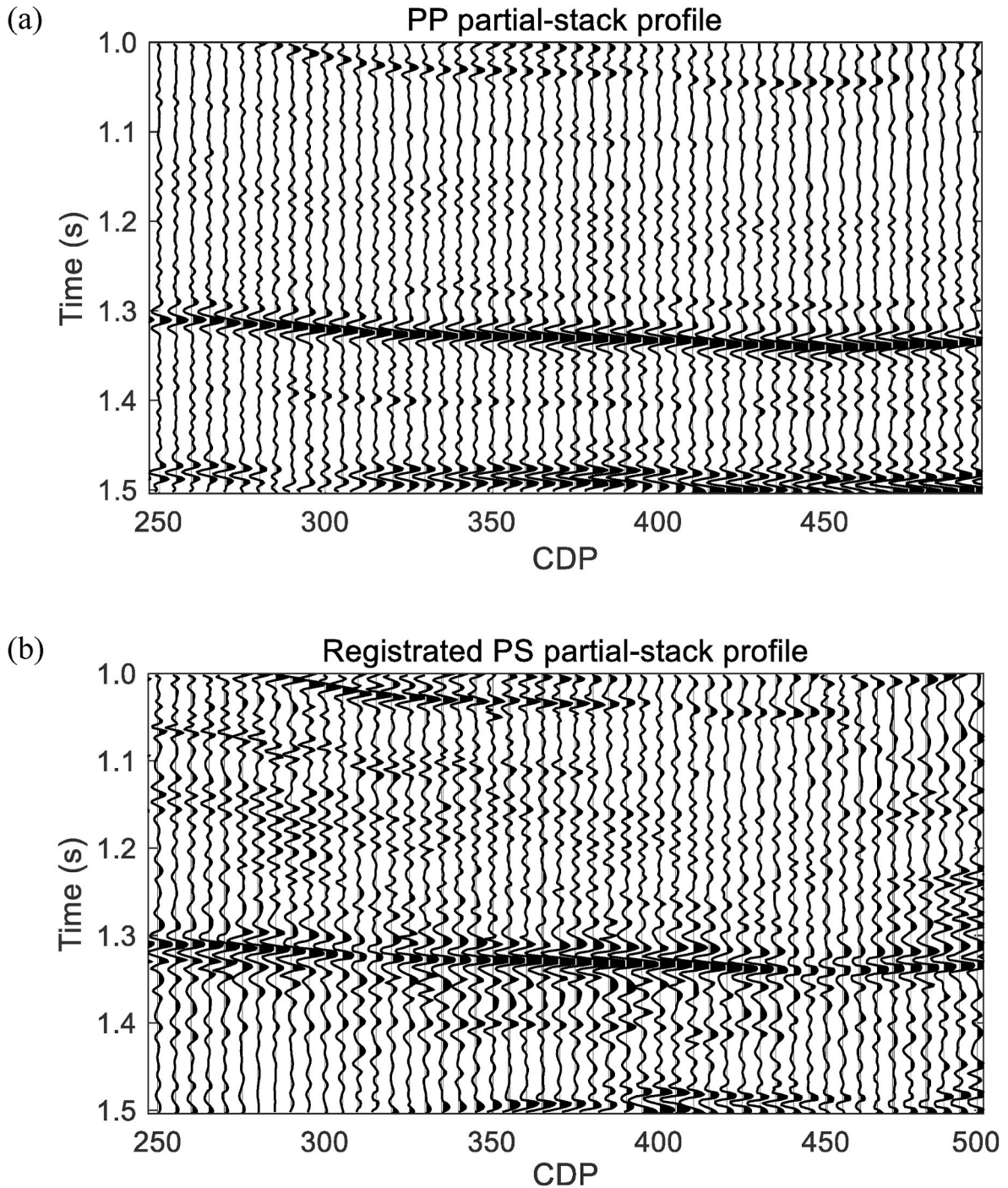


Fig. 15. (a) The constant-angle PP section of 30° and (b) the constant-angle PS section of 30° which has been compressed to PP time. A well was located at CDP 400.

(17.7942) and CC (0.9387). Compared with ϵ , the parameter δ is more susceptible to noise interference. The noise test shows the proposed joint inversion is robust on noisy data for the parameter extractions of c_{33} , c_{55} and c_{11} . However, to ensure a reliable result of ϵ , the SNR of input datasets should be sufficiently high (≥ 5). For an acceptable estimation of δ , the quality of the gathers must be ensured by using effective denoising methods (Wang et al., 2016; Chen et al., 2019).

5.3. Multi-component field data

The reservoir is a stable set of shale layers from the Sichuan Basin in Southwest China. There is a well penetrating the lower shale formation

with a depth ranging from 2000 to 2400 m at CDP 400. The anisotropy parameters ϵ and δ cannot be measured directly in the boreholes, and we predict them for the shale formation by using an effective rock-physics-based method (Zhang et al., 2017; Zhang, 2017, 2019). Based on the anisotropic effective-medium theories, the Thomsen's anisotropy parameters ϵ and δ can be calculated by using the logs of mineralogy, TOC and porosities of clay-bound water, free water and free gas. Fig. 14a shows the curves of two velocities, density and two computed anisotropy parameters. Fig. 14b shows the parameter choice of the inversion, i.e., the stiffnesses and density. The anisotropy parameters ϵ and δ indicate that the shale reservoirs (from 1.29 to 1.47 s) have moderate anisotropy. The seismic input includes a set of PP-wave angle gathers ranging from 5

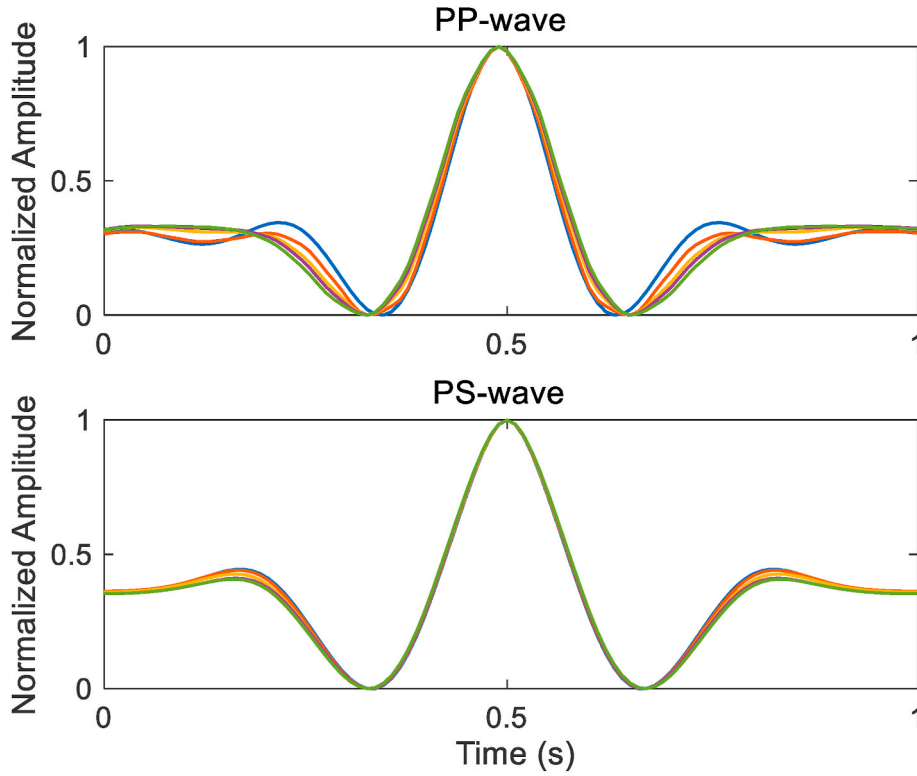


Fig. 16. Angle-dependent wavelets extracted from the real PP-wave angle gathers (upper plot) and PS-wave angle gathers (lower plot), used in the inversion process. The curves with different colors correspond to wavelets extracted from different partial stack seismic data. (For interpretation of the references to color in this figure legend, the reader is referred to the Web version of this article.)

to 45° and a set of PS-wave gathers from 5 to 35° . Before performing the anisotropic AVO inversion, the PS gathers should be compressed to the PP time. Since a multi-component inversion is greatly affected by the quality of the compressed PS gathers, an effective PP- and PS-wave matching approach is essential for the reliable joint inversion results. In this work, the dynamic time warping algorithm (Hale, 2009) is adopted to realize the PP- and PS-wave registration. Then the PP and compressed PS data within the certain angle intervals are stacked to construct the constant-angle sections (partial stacked sections), as shown in Fig. 15. The angle-dependent wavelets for the inversion are estimated from the seismic gathers, and the corresponding normalized wavelets are shown in Fig. 16, where the upper one is used to compute the PP-wave synthetics and the lower one is used for the PS-wave synthetics. Since good initial models are helpful in reducing the risk of falling into the local minimum solutions. We used a geological structure oriented method (Chen et al., 2019; Huang et al., 2020) to improve the reliability of the initial models, as shown in Fig. 17. The EGI and JEGI are adopted in the five-parameter inversion, and to obtain reliable results, the L-BFGS optimization scheme is used. A Gaussian is set as the priori constraint and the covariance matrices are computed by using the given initial models.

Figs. 18 and 20 show the 2D inversion profiles for all CDPs by using the EGI and JEGI, respectively. The corresponding well logs are included in the profiles. It can be seen that c_{33} and c_{55} are better than c_{11} and c_{13} estimated (regarding well consistency and stability). Compared with EGI, the JEGI estimation shows a better match and higher horizontal continuity. We can observe the improvement of the horizontal continuity in the profiles of c_{11} , c_{13} and density. The areas with better lateral continuities are highlighted by black arrows in Fig. 20. Figs. 19 and 21 show the computed profiles of the anisotropy parameters ϵ and δ with the inversion results of Figs. 18 and 20, respectively. The better estimation of JEGI yields better results of both anisotropy parameters. According to the local conditions, the results obtained with JEGI are in

better agreement with the geological structure.

Fig. 22a and b shows the EGI and JEGI inversions by using traces near the well, respectively. For EGI, c_{33} has the best estimation, followed by c_{55} and c_{11} , while the results for c_{13} and density are not satisfactory. The corresponding CCs and RMSEs are shown in Table 8. Fig. 22b shows that the estimations with JEGI of the five parameters are in better agreement with the well logs. The accuracy of c_{13} and density is highly improved by the proposed joint inversion. Compared with the CCs of EGI: 0.8350 (c_{13}) and 0.7154 (density), those of JEGI are higher, i.e., 0.9234 (c_{13}) and 0.8349 (density). JEGI shows a better performance, especially for c_{13} and density. Fig. 23a and b shows the computed anisotropy parameters ϵ and δ at the well location by using the results of Fig. 22a and b, respectively. The CCs and RMSEs between the computed anisotropy parameters and well logs are shown in Table 9, which demonstrates the effectiveness of JEGI. Moreover, the 2D profiles validate the horizontal continuity. However, compared with ϵ , even using the joint inversion, acceptable results of δ cannot be obtained. Further studies are needed to solve this problem.

6. Conclusions

We have developed a joint PP and PS pre-stack AVA inversion, using the exact Graebner equation as forward engine, which effectively improves the inversion stability and accuracy of the anisotropy parameters ϵ and δ for VTI media. The set $\{c_{33}, c_{55}, c_{11}, c_{13}, \rho\}$ is considered as parameter of the inversion. The sensitivity analysis shows that, compared with the commonly used parameter choice $\{V_p, V_s, \rho, \epsilon, \delta\}$, the above choice has higher sensitivity to seismic amplitudes for anisotropy-related parameters (c_{11} and c_{13}) and smaller sensitivity gap between velocity- (c_{33} and c_{55}) and anisotropy-related parameters. That choice improves the accuracy of anisotropy-related parameters and the stability of the multi-parametric inversion. By using the L-BFGS optimization, the joint inversion algorithm can reliably invert four stiffness

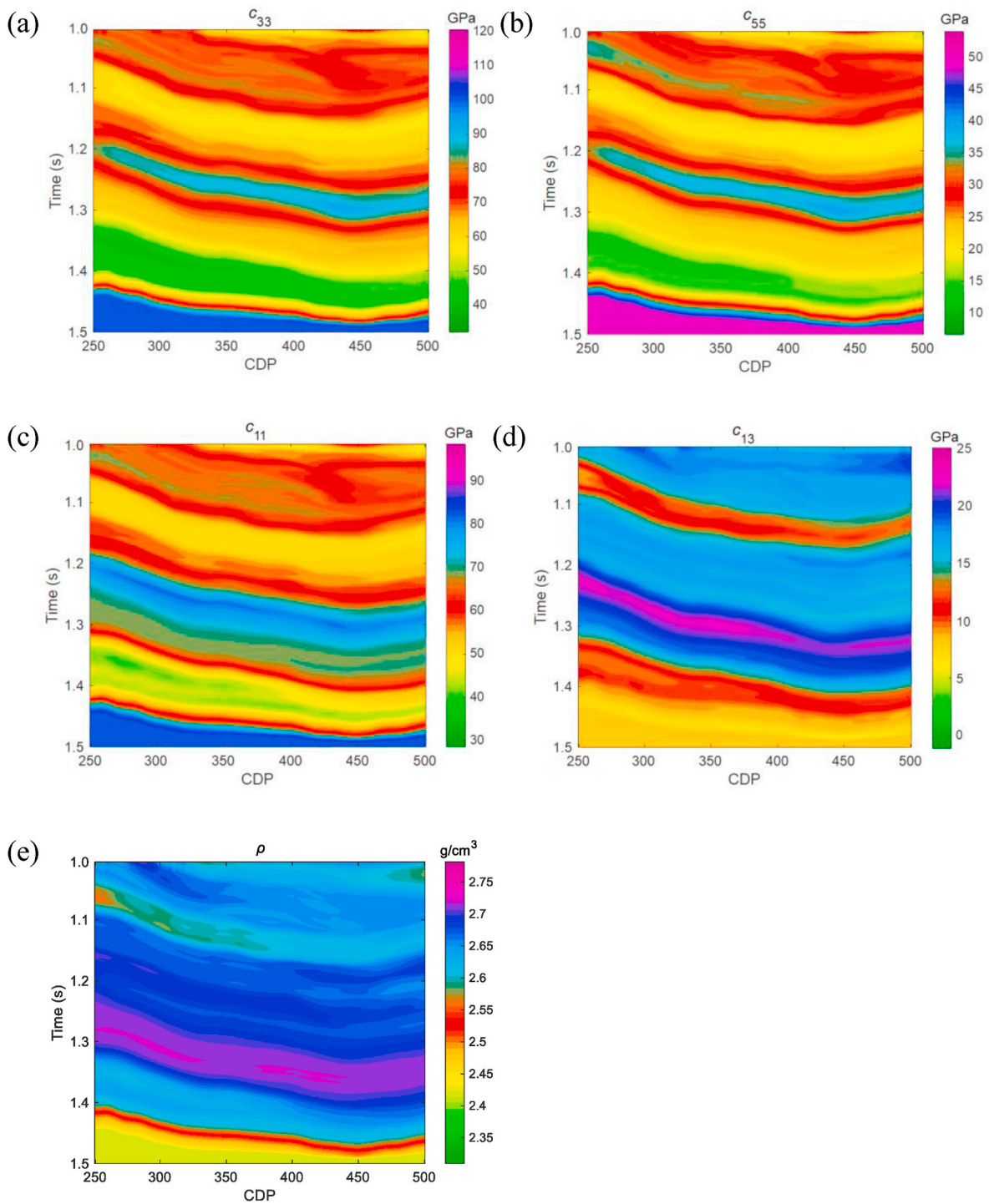


Fig. 17. The initial models which are used in the inversion tests, namely, (a) c_{33} , (b) c_{55} , (c) c_{11} , (d) c_{13} and (e) bulk density ρ .

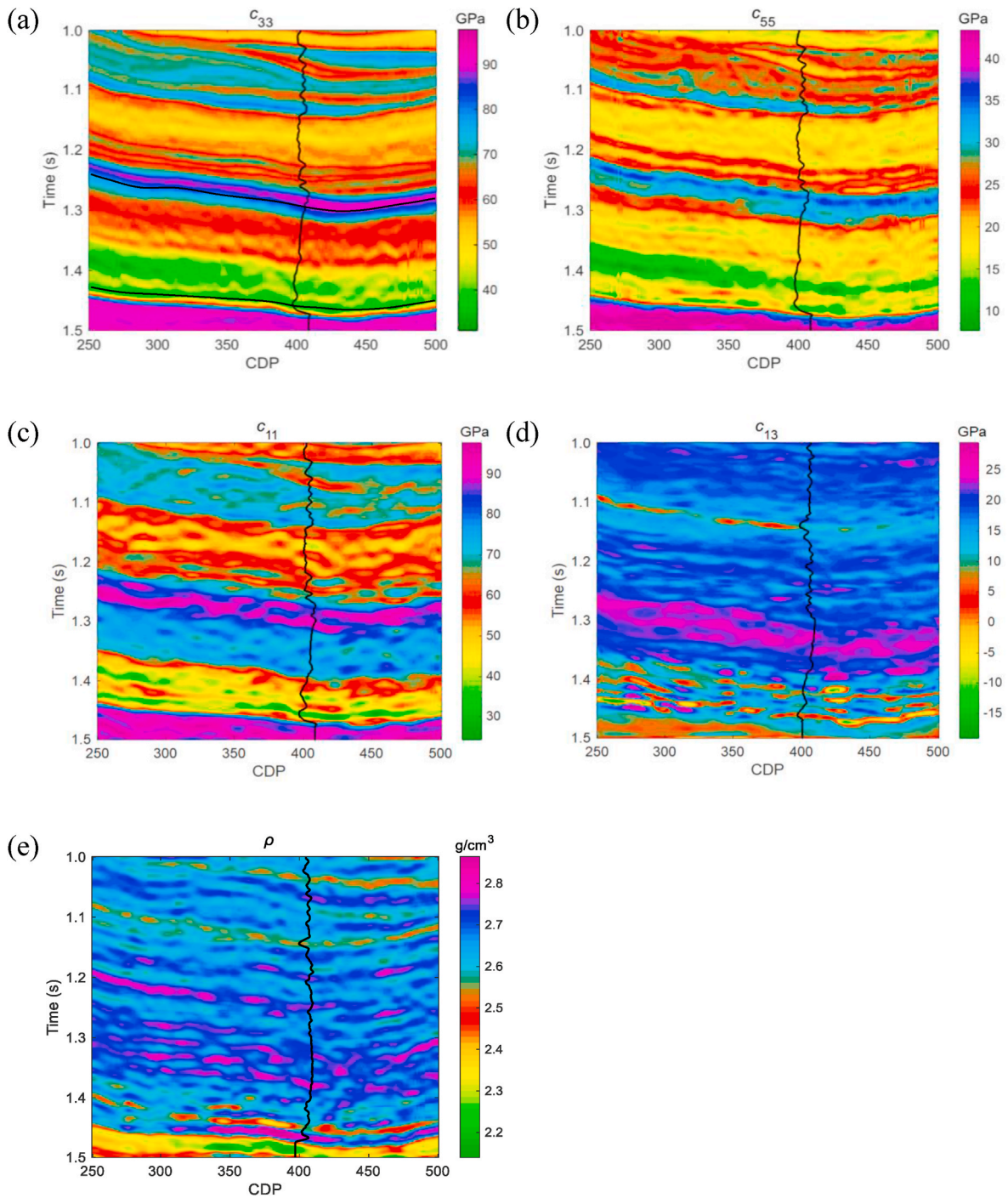


Fig. 18. Inverted sections, namely, (a) c_{33} , (b) c_{55} , (c) c_{11} , (d) c_{13} and (e) bulk density ρ by using the EGI algorithm. The corresponding well logs are given. The top and bottom interfaces of the target shale reservoir have been marked by using the black curves in Fig. 17a.

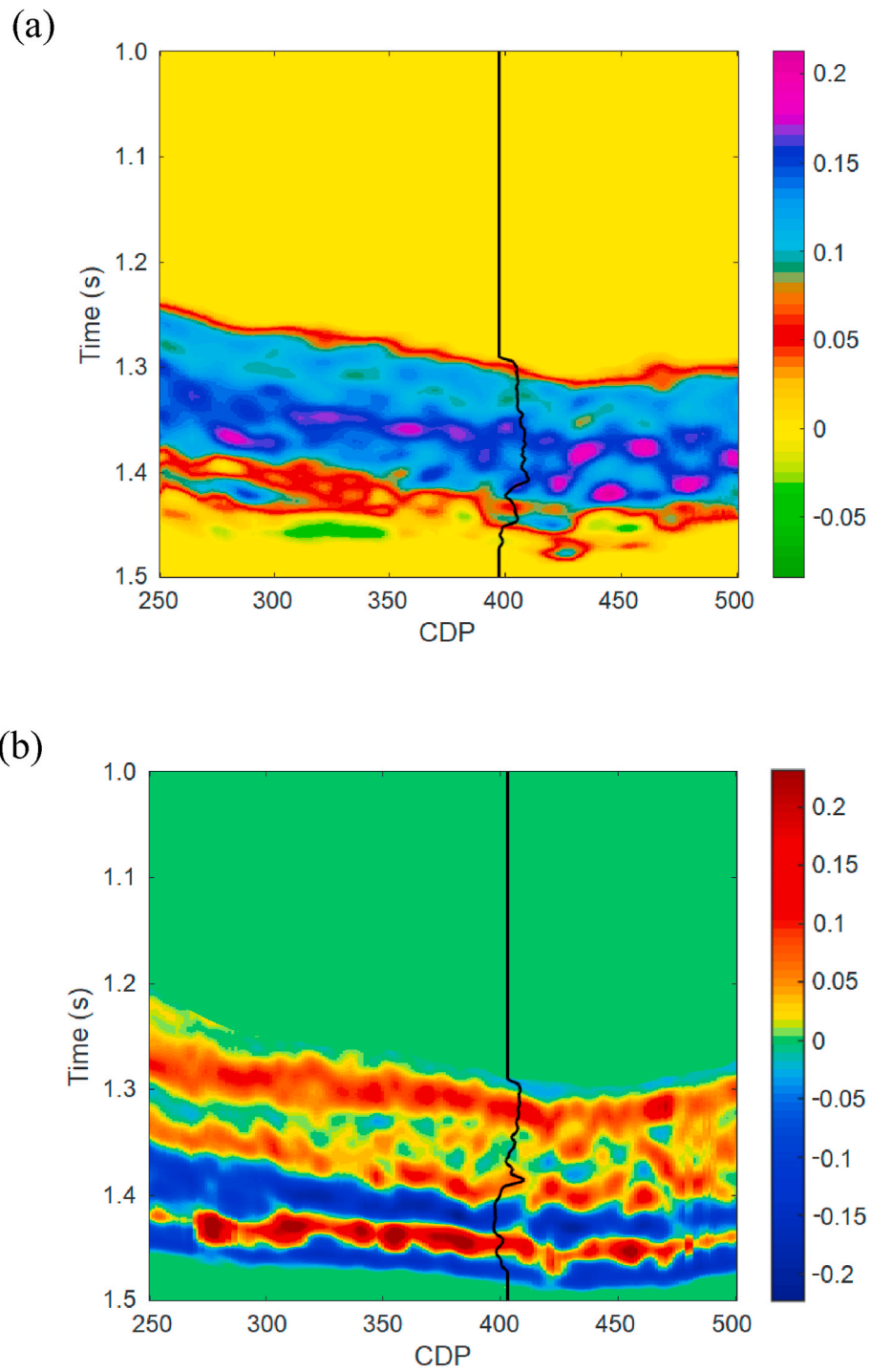


Fig. 19. Computed sections for (a) ε and (b) δ by using the results of Fig. 13. The corresponding well logs are given.

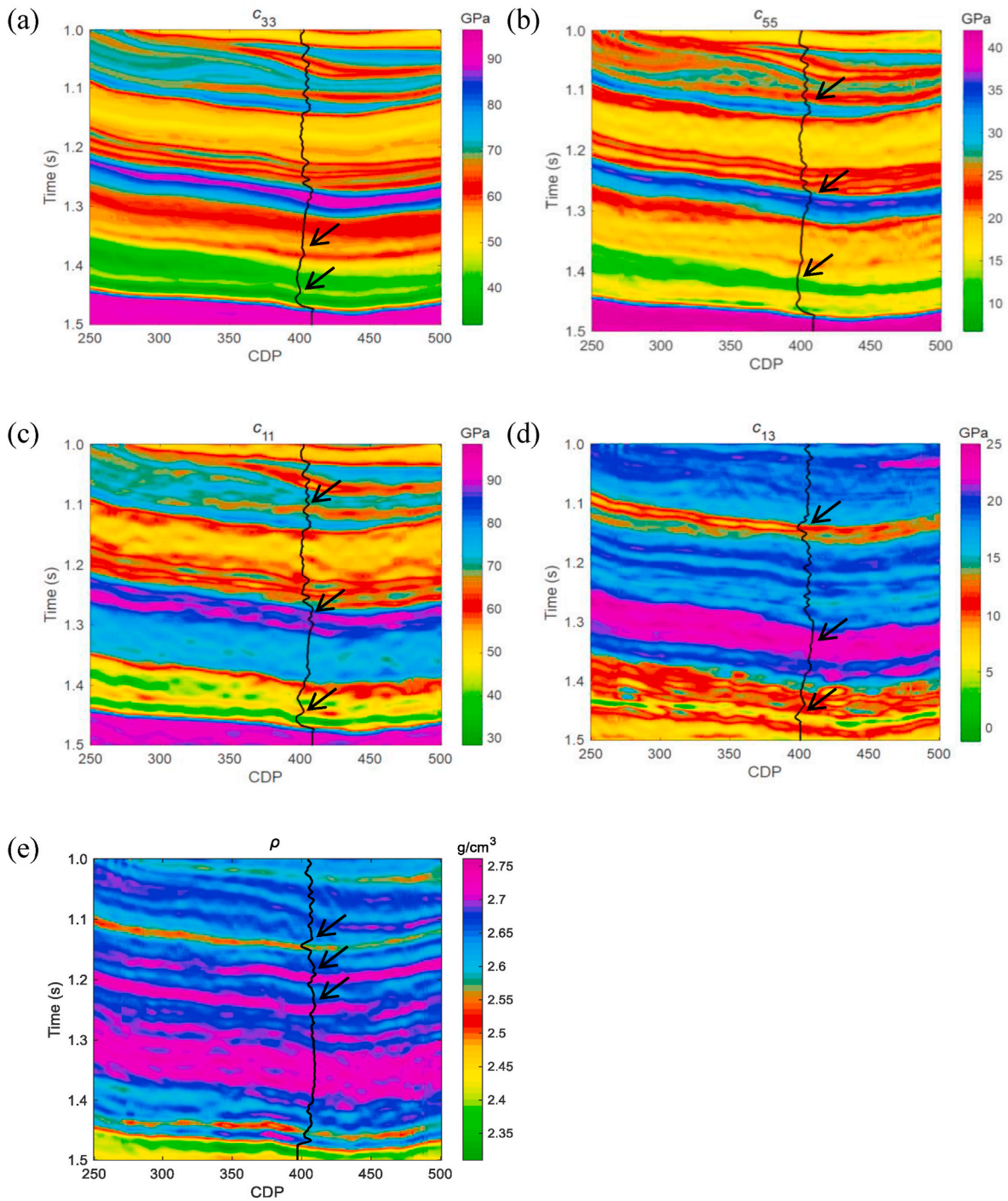


Fig. 20. Inverted sections for (a) c_{33} , (b) c_{55} , (c) c_{11} , (d) c_{13} and (e) ρ by using the JEGI algorithm. The corresponding well logs are given.

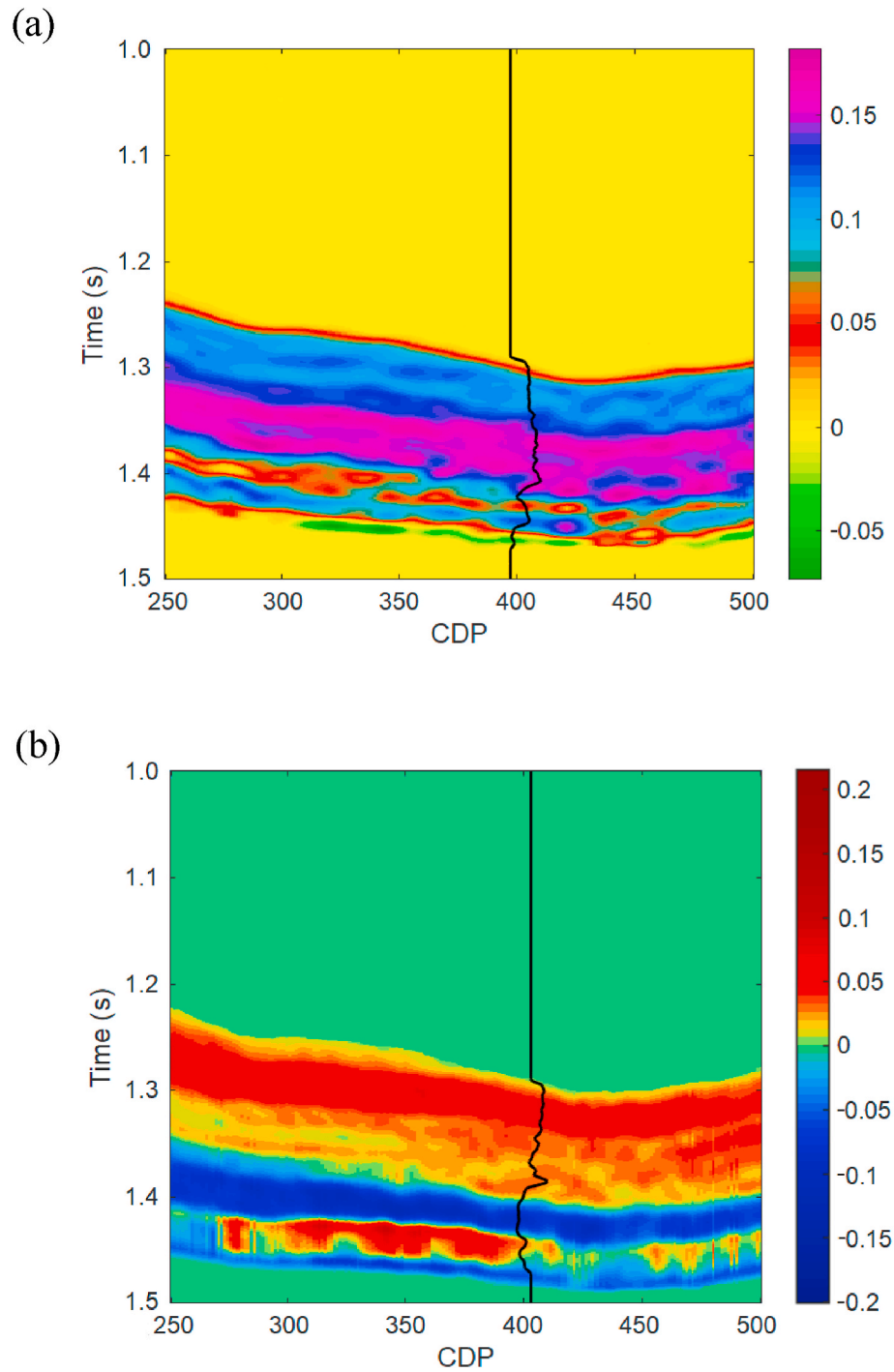


Fig. 21. Computed sections for (a) ε and (b) δ by using the results of Fig. 15. The corresponding well logs are given.

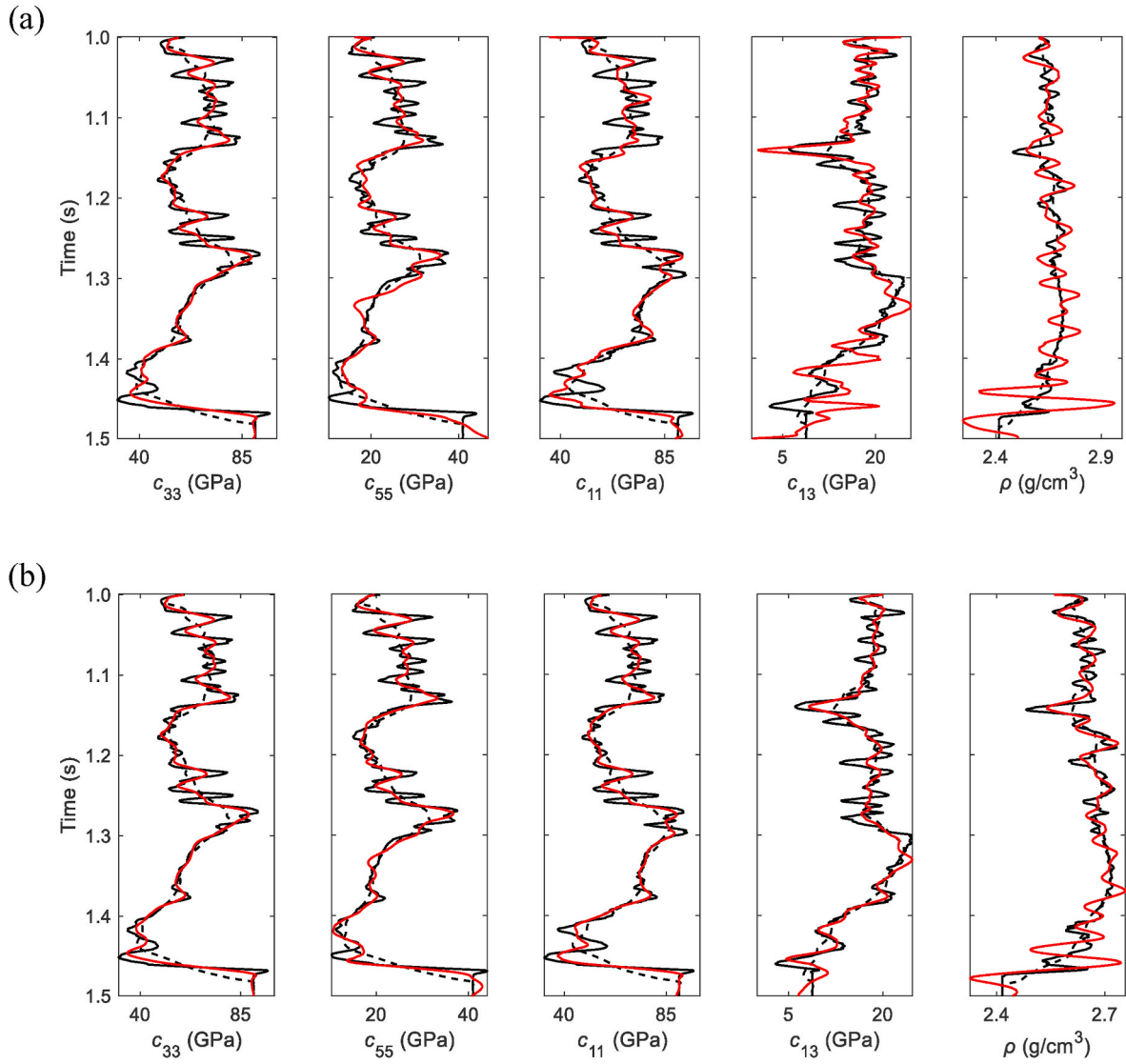


Fig. 22. Inversion results at the well location obtained with the EGI (a) and JEGI (b) algorithms. The black solid lines are the real logs, and the black dotted and red curves are the initial logs and inversion results, respectively. (For interpretation of the references to color in this figure legend, the reader is referred to the Web version of this article.)

parameters, and then the anisotropy parameters ε and δ are computed.

The proposed JEGI algorithm is tested with synthetic data and then applied to field seismic data. The test shows that the single PP-data inversion yields an acceptable ε estimation, however the results for δ

are unsatisfactory. The joint PP-PS data improves the results, especially for c_{13} and ρ , and therefore improves the δ estimation. Moreover, the 2D inverted profiles validate the horizontal continuity and stability of the JEGI algorithm.

Compared with the isotropic conditions, more parameters are expected to be obtained by the anisotropic AVO inversion, of which solutions are more easily being trapped into local minima. In the proposed JEGI, good initial models are strongly recommended to reduce the multiplicity and instability of solutions. Since the anisotropy parameter δ is more susceptible to noise interference, it is necessary to ensure the quality of the input gathers. Moreover, a nonlinear or combined linear and nonlinear inversion strategy is recommended to further improve the estimation accuracy of the anisotropic parameters, especially for δ .

Table 8

RMSE and CC between the inversion results by using seismic traces near the well and the logs by using EGI and JEGI.

Inversion results		c_{33}	c_{55}	c_{11}	c_{13}	ρ
EGI	RMSE	7.7357	11.2540	12.9754	18.2540	3.3513
	CC	0.9401	0.9182	0.9034	0.8350	0.7154
JEGI	RMSE	6.7317	7.8699	8.1225	9.5833	1.7635
	CC	0.9532	0.9489	0.9398	0.9234	0.8349

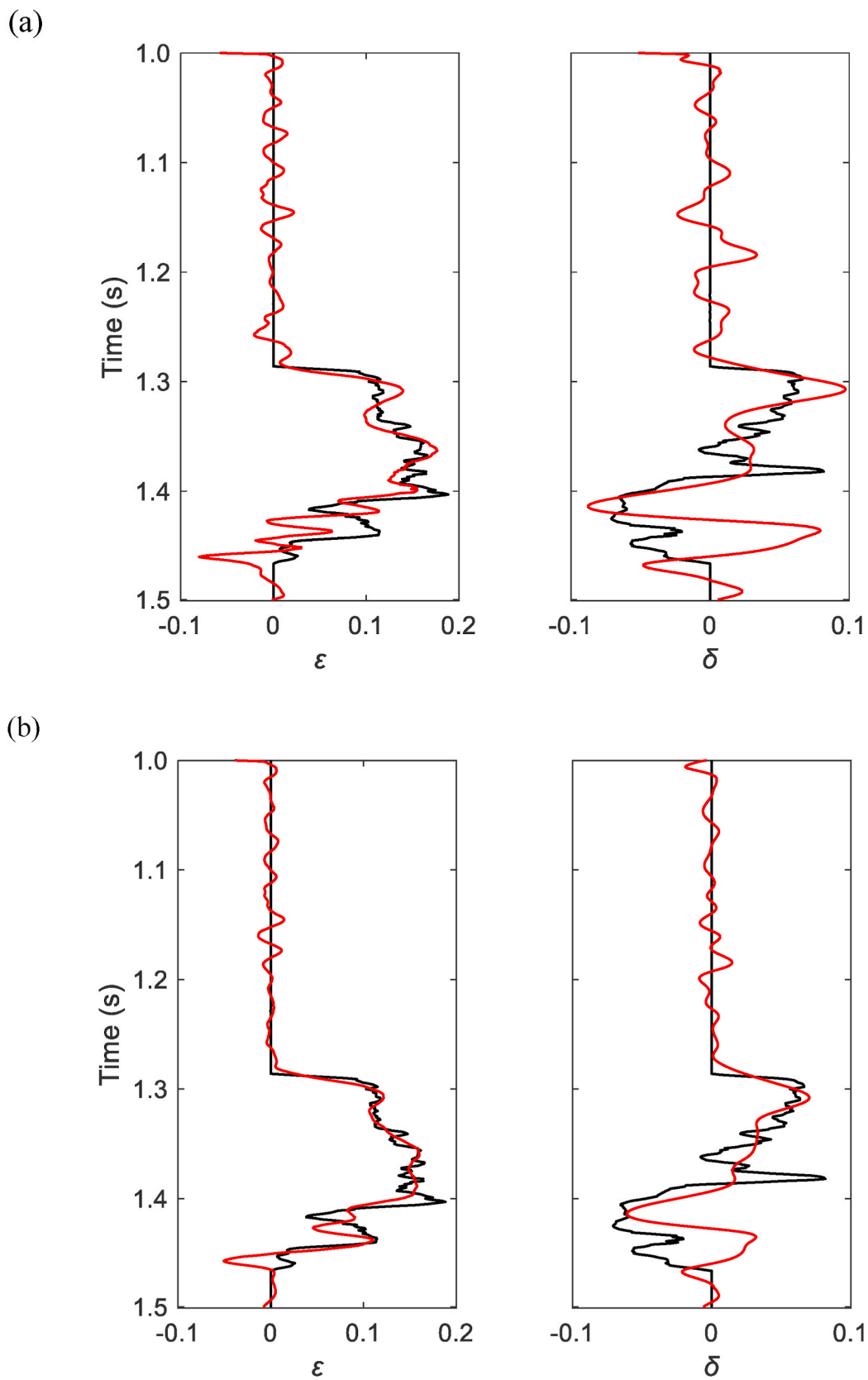


Fig. 23. Computed anisotropy parameters at the well location by using the results of Fig. 17; (a) EGI (Fig. 15a); (b) JEGI (Fig. 15b). The black solid lines are the real logs and the red curves are the computed results. (For interpretation of the references to color in this figure legend, the reader is referred to the Web version of this article.)

Table 9

RMSE and CC between the computed anisotropy parameters in field data application and the well logs by using EGI and JEGI.

Inversion results		ϵ	δ
EGI	RMSE	14.4888	33.82
	CC	0.8745	0.7096
JEGI	RMSE	8.6202	19.82
	CC	0.9263	0.8212

Declaration of competing interest

The authors declare that they have no known competing financial interests or personal relationships that could have appeared to influence the work reported in this paper.

APPENDIX

Derivations of matrices \mathbf{S} and \mathbf{b}

We take $(c_{11})_1$ as an example here. The derivatives with respect to the stiffness parameters of the upper layer $(c_{33})_1, (c_{55})_1$ have similar forms. According to equations (3) and (5), we have

$$\frac{\partial \mathbf{S}}{\partial (c_{11})_1} = \begin{bmatrix} \frac{\partial \ell_{1P}}{\partial (c_{11})_1} & \frac{\partial n_{1S}}{\partial (c_{11})_1} & 0 & 0 \\ \frac{\partial n_{1P}}{\partial (c_{11})_1} & \frac{\partial \ell_{1S}}{\partial (c_{11})_1} & 0 & 0 \\ \frac{\partial a_1}{\partial (c_{11})_1} & \frac{\partial b_1}{\partial (c_{11})_1} & 0 & 0 \\ \frac{\partial d_1}{\partial (c_{11})_1} & \frac{\partial e_1}{\partial (c_{11})_1} & 0 & 0 \end{bmatrix} \quad (\text{A-1})$$

and

$$\frac{\partial \mathbf{b}}{\partial (c_{11})_1} = \left[-\frac{\partial \ell_{1P}}{\partial (c_{11})_1} \quad \frac{\partial n_{1P}}{\partial (c_{11})_1} \quad E_{(c_{11})_1} \quad H_{(c_{11})_1} \right]^T, \quad (\text{A-2})$$

where

$$\frac{\partial a_1}{\partial (c_{11})_1} = (c_{55})_1 \cdot \left(\frac{\partial s_{1P}}{\partial (c_{11})_1} \ell_{1P} + s_{1P} \frac{\partial \ell_{1P}}{\partial (c_{11})_1} + \frac{\partial p}{\partial (c_{11})_1} n_{1P} + p \frac{\partial n_{1P}}{\partial (c_{11})_1} \right), \quad (\text{A-3})$$

$$\frac{\partial b_1}{\partial (c_{11})_1} = (c_{55})_1 \cdot \left(\frac{\partial s_{1S}}{\partial (c_{11})_1} n_{1S} + s_{1S} \frac{\partial n_{1S}}{\partial (c_{11})_1} - \frac{\partial p}{\partial (c_{11})_1} \ell_{1S} - p \frac{\partial \ell_{1S}}{\partial (c_{11})_1} \right), \quad (\text{A-4})$$

$$\frac{\partial d_1}{\partial (c_{11})_1} = (c_{13})_1 \cdot \left(\ell_{1P} \frac{\partial p}{\partial (c_{11})_1} + p \frac{\partial \ell_{1P}}{\partial (c_{11})_1} \right) + (c_{33})_1 \cdot \left(n_{1P} \frac{\partial s_{1P}}{\partial (c_{11})_1} + s_{1P} \frac{\partial n_{1P}}{\partial (c_{11})_1} \right), \quad (\text{A-5})$$

$$\frac{\partial e_1}{\partial (c_{11})_1} = (c_{13})_1 \cdot \left(n_{1S} \frac{\partial p}{\partial (c_{11})_1} + p \frac{\partial n_{1S}}{\partial (c_{11})_1} \right) - (c_{33})_1 \cdot \left(\ell_{1S} \frac{\partial s_{1S}}{\partial (c_{11})_1} + s_{1S} \frac{\partial \ell_{1S}}{\partial (c_{11})_1} \right), \quad (\text{A-6})$$

$$E_{(c_{11})_1} = (c_{55})_1 \cdot \left(\frac{\partial s_{1P}}{\partial (c_{11})_1} \ell_{1P} + s_{1P} \frac{\partial \ell_{1P}}{\partial (c_{11})_1} + n_{1P} \frac{\partial p}{\partial (c_{11})_1} + p \frac{\partial n_{1P}}{\partial (c_{11})_1} \right), \quad (\text{A-7})$$

$$H_{(c_{11})_1} = -(c_{13})_1 \ell_{1P} \frac{\partial p}{\partial (c_{11})_1} - (c_{13})_1 p \frac{\partial \ell_{1P}}{\partial (c_{11})_1} - (c_{33})_1 n_{1P} \frac{\partial s_{1P}}{\partial (c_{11})_1} - (c_{33})_1 s_{1P} \frac{\partial n_{1P}}{\partial (c_{11})_1} \quad (\text{A-8})$$

with

CRedit authorship contribution statement

Cong Luo: Methodology, Software, Writing - original draft, Funding acquisition. **Jing Ba:** Conceptualization, Supervision, Funding acquisition. **José M. Carcione:** Conceptualization, Supervision, Writing - review & editing. **Guangtan Huang:** Validation, Formal analysis. **Qiang Guo:** Writing - review & editing.

Acknowledgement

The authors are grateful to the support of the Jiangsu Innovation and Entrepreneurship Plan, the China Postdoctoral Science Foundation (Grant No. 2019M661716), the Fundamental Research Funds for the Central Universities, China (Grant No. B200202135), and the National Natural Science Foundation of China (Grant No. 41974123).

$$\frac{\partial \mathcal{L}_{1P}}{\partial (c_{11})_1} = \frac{1}{2\mathcal{L}_{1P}} \left\{ \frac{2(c_{33})_1 s_{1P} \frac{\partial s_{1P}}{\partial (c_{11})_1} + 2(c_{55})_1 P \frac{\partial P}{\partial (c_{11})_1} \cdot [(c_{55})_1 \cdot (s_{1P}^2 + p^2) + (c_{11})_1 p^2 + (c_{33})_1 s_{1P}^2 - 2\rho_1] - [(c_{33})_1 s_{1P}^2 + (c_{55})_1 p^2 - \rho_1] \cdot [2(c_{55})_1 s_{1P} \frac{\partial s_{1P}}{\partial (c_{11})_1} + p^2 + 2(c_{11})_1 P \frac{\partial P}{\partial (c_{11})_1} + 2(c_{33})_1 s_{1P} \frac{\partial s_{1P}}{\partial (c_{11})_1} + 2(c_{55})_1 P \frac{\partial P}{\partial (c_{11})_1}]}{[(c_{55})_1 s_{1P}^2 + (c_{11})_1 p^2 + (c_{33})_1 s_{1P}^2 + (c_{55})_1 p^2 - 2\rho_1]} \right\}, \quad (\text{A-9})$$

$$\frac{\partial \mathcal{L}_{1P}}{\partial (c_{11})_1} = \frac{1}{2n_{1P}} \left\{ \frac{2(c_{55})_1 s_{1P} \frac{\partial s_{1P}}{\partial (c_{11})_1} + p^2 + 2(c_{11})_1 P \frac{\partial P}{\partial (c_{11})_1} \cdot [(c_{55})_1 \cdot (s_{1P}^2 + p^2) + (c_{11})_1 p^2 + (c_{33})_1 s_{1P}^2 - 2\rho_1] - [(c_{55})_1 s_{1P}^2 + (c_{11})_1 p^2 - \rho_1] \cdot [2(c_{55})_1 s_{1P} \frac{\partial s_{1P}}{\partial (c_{11})_1} + p^2 + 2(c_{11})_1 P \frac{\partial P}{\partial (c_{11})_1} + 2(c_{33})_1 s_{1P} \frac{\partial s_{1P}}{\partial (c_{11})_1} + 2(c_{55})_1 P \frac{\partial P}{\partial (c_{11})_1}]}{[(c_{55})_1 s_{1P}^2 + (c_{11})_1 p^2 + (c_{33})_1 s_{1P}^2 + (c_{55})_1 p^2 - 2\rho_1]} \right\}, \quad (\text{A-10})$$

$$\frac{\partial \mathcal{L}_{1S}}{\partial (c_{11})_1} = \frac{1}{2\mathcal{L}_{1S}} \left\{ \frac{2(c_{55})_1 s_{1S} \frac{\partial s_{1S}}{\partial (c_{11})_1} + p^2 + 2(c_{11})_1 P \frac{\partial P}{\partial (c_{11})_1} \cdot [(c_{55})_1 \cdot (s_{1S}^2 + p^2) + (c_{11})_1 p^2 + (c_{33})_1 s_{1S}^2 - 2\rho_1] - [(c_{55})_1 s_{1S}^2 + (c_{11})_1 p^2 - \rho_1] \cdot [2(c_{55})_1 s_{1S} \frac{\partial s_{1S}}{\partial (c_{11})_1} + p^2 + 2(c_{11})_1 P \frac{\partial P}{\partial (c_{11})_1} + 2(c_{33})_1 s_{1S} \frac{\partial s_{1S}}{\partial (c_{11})_1} + 2(c_{55})_1 P \frac{\partial P}{\partial (c_{11})_1}]}{[(c_{55})_1 s_{1S}^2 + (c_{11})_1 p^2 + (c_{33})_1 s_{1S}^2 + (c_{55})_1 p^2 - 2\rho_1]} \right\}, \quad (\text{A-11})$$

$$\frac{\partial n_{1S}}{\partial (c_{11})_1} = \frac{1}{2n_{1S}} \left\{ \frac{2(c_{33})_1 s_{1S} \frac{\partial s_{1S}}{\partial (c_{11})_1} + 2(c_{55})_1 P \frac{\partial P}{\partial (c_{11})_1} \cdot [(c_{55})_1 \cdot (s_{1S}^2 + p^2) + (c_{11})_1 p^2 + (c_{33})_1 s_{1S}^2 - 2\rho_1] - [(c_{33})_1 s_{1S}^2 + (c_{55})_1 p^2 - \rho_1] \cdot [2(c_{55})_1 s_{1S} \frac{\partial s_{1S}}{\partial (c_{11})_1} + p^2 + 2(c_{11})_1 P \frac{\partial P}{\partial (c_{11})_1} + 2(c_{33})_1 s_{1S} \frac{\partial s_{1S}}{\partial (c_{11})_1} + 2(c_{55})_1 P \frac{\partial P}{\partial (c_{11})_1}]}{[(c_{55})_1 s_{1S}^2 + (c_{11})_1 p^2 + (c_{33})_1 s_{1S}^2 + (c_{55})_1 p^2 - 2\rho_1]} \right\}. \quad (\text{A-12})$$

Differentiating equations (6) and (7) with respect to $(c_{11})_1$, we obtain the expressions of $\frac{\partial s_{1p}}{\partial (c_{11})_1}$ and $\frac{\partial s_{1s}}{\partial (c_{11})_1}$.
 Let us consider $(c_{11})_2$. Then,

$$\frac{\partial \mathbf{S}}{\partial (c_{11})_2} = \begin{bmatrix} 0 & 0 & \frac{\partial \ell_{2p}}{\partial (c_{11})_2} & \frac{\partial n_{2s}}{\partial (c_{11})_2} \\ 0 & 0 & \frac{\partial n_{2p}}{\partial (c_{11})_2} & \frac{\partial \ell_{2s}}{\partial (c_{11})_2} \\ 0 & 0 & \frac{\partial a_2}{\partial (c_{11})_2} & \frac{\partial b_2}{\partial (c_{11})_2} \\ 0 & 0 & \frac{\partial d_2}{\partial (c_{11})_2} & \frac{\partial e_2}{\partial (c_{11})_2} \end{bmatrix}, \quad (\text{A-13})$$

where the derivatives of the lower layer $\frac{\partial a_2}{\partial (c_{11})_2}$, $\frac{\partial b_2}{\partial (c_{11})_2}$, $\frac{\partial d_2}{\partial (c_{11})_2}$, $\frac{\partial e_2}{\partial (c_{11})_2}$, $\frac{\partial \ell_{2p}}{\partial (c_{11})_2}$, $\frac{\partial n_{2p}}{\partial (c_{11})_2}$, $\frac{\partial \ell_{2s}}{\partial (c_{11})_2}$, and $\frac{\partial n_{2s}}{\partial (c_{11})_2}$ have the same forms as those of the upper layer (see equations (A-3) to (A-6) and equations (A-9) to (A-11)). The expressions for the stiffness parameters of the lower layer $(c_{33})_2$, $(c_{55})_2$ have similar forms.

To compute $\frac{\partial \mathbf{r}}{\partial (c_{13})_1}$ in equation (26), we differentiate equations (3) and (5) and obtain

$$\frac{\partial \mathbf{S}}{\partial (c_{13})_1} = \begin{bmatrix} 0 & 0 & 0 & 0 \\ 0 & 0 & 0 & 0 \\ 0 & 0 & 0 & 0 \\ \frac{\partial d_1}{\partial (c_{13})_1} & \frac{\partial e_1}{\partial (c_{13})_1} & 0 & 0 \end{bmatrix} \quad (\text{A-14})$$

and

$$\frac{\partial \mathbf{b}}{\partial (c_{13})_1} = [0 \quad 0 \quad 0 \quad H_{(c_{13})_1}]^T, \quad (\text{A-15})$$

where

$$\frac{\partial d_1}{\partial (c_{13})_1} = \ell_{1p} p, \quad (\text{A-16})$$

$$\frac{\partial e_1}{\partial (c_{13})_1} = n_{1s} p, \quad (\text{A-17})$$

$$H_{(c_{13})_1} = -\ell_{1p} p. \quad (\text{A-18})$$

The derivative of matrix \mathbf{S} with respect to the lower medium parameter $(c_{13})_2$ in equation (27) is

$$\frac{\partial \mathbf{S}}{\partial (c_{13})_2} = \begin{bmatrix} 0 & 0 & 0 & 0 \\ 0 & 0 & 0 & 0 \\ 0 & 0 & 0 & 0 \\ 0 & 0 & \frac{\partial d_2}{\partial (c_{13})_2} & \frac{\partial e_2}{\partial (c_{13})_2} \end{bmatrix} \quad (\text{A-19})$$

with

$$\frac{\partial d_2}{\partial (c_{13})_2} = \ell_{2P} p, \quad (\text{A-20})$$

$$\frac{\partial e_2}{\partial (c_{13})_2} = n_{2S} p. \quad (\text{A-21})$$

Regarding the bulk density of the upper medium ρ_1 , the partial derivatives $\frac{\partial \mathbf{S}}{\partial \rho_1}$ and $\frac{\partial \mathbf{b}}{\partial \rho_1}$ in equation (32) are

$$\frac{\partial \mathbf{S}}{\partial \rho_1} = \begin{bmatrix} \frac{\partial \ell_{1P}}{\partial \rho_1} & \frac{\partial n_{1S}}{\partial \rho_1} & 0 & 0 \\ \frac{\partial n_{1P}}{\partial \rho_1} & \frac{\partial \ell_{1S}}{\partial \rho_1} & 0 & 0 \\ \frac{\partial a_1}{\partial \rho_1} & \frac{\partial b_1}{\partial \rho_1} & 0 & 0 \\ \frac{\partial d_1}{\partial \rho_1} & \frac{\partial e_1}{\partial \rho_1} & 0 & 0 \end{bmatrix} \quad (\text{A-22})$$

and

$$\frac{\partial \mathbf{b}}{\partial \rho_1} = \left[-\frac{\partial \ell_{1P}}{\partial \rho_1} \quad \frac{\partial n_{1P}}{\partial \rho_1} \quad E_{\rho_1} \quad H_{\rho_1} \right]^T, \quad (\text{A-23})$$

where

$$\frac{\partial a_1}{\partial \rho_1} = (c_{55})_1 \cdot \left(\frac{\partial s_{1P}}{\partial \rho_1} \ell_{1P} + s_{1P} \frac{\partial \ell_{1P}}{\partial \rho_1} + \frac{\partial p}{\partial \rho_1} n_{1P} + p \frac{\partial n_{1P}}{\partial \rho_1} \right), \quad (\text{A-24})$$

$$\frac{\partial b_1}{\partial \rho_1} = (c_{55})_1 \cdot \left(\frac{\partial s_{1S}}{\partial \rho_1} n_{1S} + s_{1S} \frac{\partial n_{1S}}{\partial \rho_1} - \ell_{1S} \frac{\partial p}{\partial \rho_1} - p \frac{\partial \ell_{1S}}{\partial \rho_1} \right), \quad (\text{A-25})$$

$$\frac{\partial d_1}{\partial \rho_1} = (c_{13})_1 \cdot \left(\ell_{1P} \frac{\partial p}{\partial \rho_1} + p \frac{\partial \ell_{1P}}{\partial \rho_1} \right) + (c_{33})_1 \cdot \left(n_{1P} \frac{\partial s_{1P}}{\partial \rho_1} + s_{1P} \frac{\partial n_{1P}}{\partial \rho_1} \right), \quad (\text{A-26})$$

$$\frac{\partial e_1}{\partial \rho_1} = (c_{13})_1 \cdot \left(n_{1S} \frac{\partial p}{\partial \rho_1} + p \frac{\partial n_{1S}}{\partial \rho_1} \right) - (c_{33})_1 \cdot \left(\ell_{1S} \frac{\partial s_{1S}}{\partial \rho_1} + s_{1S} \frac{\partial \ell_{1S}}{\partial \rho_1} \right), \quad (\text{A-27})$$

$$E_{\rho_1} = (c_{55})_1 \cdot \left(\frac{\partial s_{1P}}{\partial \rho_1} \ell_{1P} + s_{1P} \frac{\partial \ell_{1P}}{\partial \rho_1} + n_{1P} \frac{\partial p}{\partial \rho_1} + p \frac{\partial n_{1P}}{\partial \rho_1} \right), \quad (\text{A-28})$$

$$H_{\rho_1} = - (c_{13})_1 \cdot \left(\ell_{1P} \frac{\partial p}{\partial \rho_1} + p \frac{\partial \ell_{1P}}{\partial \rho_1} \right) - (c_{33})_1 \cdot \left(n_{1P} \frac{\partial s_{1P}}{\partial \rho_1} + s_{1P} \frac{\partial n_{1P}}{\partial \rho_1} \right), \quad (\text{A-29})$$

with

$$\frac{\partial \mathcal{L}_{1P}}{\partial \rho_1} = \frac{1}{2\mathcal{L}_{1P}} \left\{ \frac{2(c_{33})_1 s_{1P} \frac{\partial s_{1P}}{\partial \rho_1} + p^2 + 2(c_{55})_1 p \frac{\partial p}{\partial \rho_1} - 1}{[(c_{55})_1 s_{1P}^2 + (c_{11})_1 p^2 + (c_{33})_1 s_{1P}^2 - 2\rho_1] - [(c_{33})_1 s_{1P}^2 + (c_{55})_1 p^2 - \rho_1]} \cdot \left[2(c_{55})_1 s_{1P} \frac{\partial s_{1P}}{\partial \rho_1} + 2(c_{11})_1 p \frac{\partial p}{\partial \rho_1} + 2(c_{33})_1 s_{1P} \frac{\partial s_{1P}}{\partial \rho_1} + 2(c_{55})_1 p \frac{\partial p}{\partial \rho_1} - 2 \right] \right\}, \quad (\text{A-30})$$

$$\frac{\partial \mathcal{L}_{1P}}{\partial \rho_1} = \frac{1}{2n_{1P}} \left\{ \frac{2(c_{55})_1 s_{1P} \frac{\partial s_{1P}}{\partial \rho_1} + 2(c_{11})_1 p \frac{\partial p}{\partial \rho_1} - 1}{[(c_{55})_1 s_{1P}^2 + (c_{11})_1 p^2 + (c_{33})_1 s_{1P}^2 - 2\rho_1] - [(c_{55})_1 s_{1P}^2 + (c_{11})_1 p^2 - \rho_1]} \cdot \left[2(c_{55})_1 s_{1P} \frac{\partial s_{1P}}{\partial \rho_1} + 2(c_{11})_1 p \frac{\partial p}{\partial \rho_1} + 2(c_{33})_1 s_{1P} \frac{\partial s_{1P}}{\partial \rho_1} + 2(c_{55})_1 p \frac{\partial p}{\partial \rho_1} - 2 \right] \right\}, \quad (\text{A-31})$$

$$\frac{\partial \mathcal{L}_{1S}}{\partial \rho_1} = \frac{1}{2\mathcal{L}_{1S}} \left\{ \frac{2(c_{55})_1 s_{1S} \frac{\partial s_{1S}}{\partial (c_{55})_1} + 2(c_{11})_1 p \frac{\partial p}{\partial (c_{55})_1} - 1}{[(c_{55})_1 s_{1S}^2 + (c_{11})_1 p^2 + (c_{33})_1 s_{1S}^2 - 2\rho_1] - [(c_{55})_1 s_{1S}^2 + (c_{11})_1 p^2 - \rho_1]} \cdot \left[2(c_{55})_1 s_{1S} \frac{\partial s_{1S}}{\partial \rho_1} + 2(c_{11})_1 p \frac{\partial p}{\partial \rho_1} + 2(c_{33})_1 s_{1S} \frac{\partial s_{1S}}{\partial \rho_1} + 2(c_{55})_1 p \frac{\partial p}{\partial \rho_1} - 2 \right] \right\}, \quad (\text{A-32})$$

$$\frac{\partial n_{1S}}{\partial \rho_1} = \frac{1}{2n_{1S}} \left\{ \frac{2(c_{33})_1 s_{1S} \frac{\partial s_{1S}}{\partial \rho_1} + 2(c_{55})_1 p \frac{\partial p}{\partial (c_{55})_1} - 1}{[(c_{55})_1 s_{1S}^2 + (c_{11})_1 p^2 + (c_{33})_1 s_{1S}^2 + (c_{55})_1 p^2 - 2\rho_1] - [(c_{33})_1 s_{1S}^2 + (c_{55})_1 p^2 - \rho_1]} \cdot \left[2(c_{55})_1 s_{1S} \frac{\partial s_{1S}}{\partial \rho_1} + 2(c_{11})_1 p \frac{\partial p}{\partial \rho_1} + 2(c_{33})_1 s_{1S} \frac{\partial s_{1S}}{\partial \rho_1} + 2(c_{55})_1 p \frac{\partial p}{\partial \rho_1} - 2 \right] \right\}. \quad (\text{A-33})$$

Differentiating equations (6) and (7) with respect to the bulk density ρ_1 , we obtain the expressions $\frac{\partial s_{1P}}{\partial \rho_1}$ and $\frac{\partial s_{1S}}{\partial \rho_1}$.

Regarding the lower medium, the derivative of matrix \mathbf{S} with respect to ρ_2 in equation (33) is

$$\frac{\partial \mathbf{S}}{\partial \rho_2} = \begin{bmatrix} 0 & 0 & \frac{\partial \ell_{2P}}{\partial \rho_2} & \frac{\partial n_{2S}}{\partial \rho_2} \\ 0 & 0 & \frac{\partial n_{2P}}{\partial \rho_2} & \frac{\partial \ell_{2S}}{\partial \rho_2} \\ 0 & 0 & \frac{\partial a_2}{\partial \rho_2} & \frac{\partial b_2}{\partial \rho_2} \\ 0 & 0 & \frac{\partial d_2}{\partial \rho_2} & \frac{\partial e_2}{\partial \rho_2} \end{bmatrix}, \quad (\text{A-34})$$

where $\frac{\partial a_2}{\partial \rho_2}$, $\frac{\partial b_2}{\partial \rho_2}$, $\frac{\partial d_2}{\partial \rho_2}$, $\frac{\partial e_2}{\partial \rho_2}$, $\frac{\partial \ell_{2P}}{\partial \rho_2}$, $\frac{\partial n_{2P}}{\partial \rho_2}$, $\frac{\partial \ell_{2S}}{\partial \rho_2}$, $\frac{\partial n_{2S}}{\partial \rho_2}$ have the same form as those with respect to the upper layer parameter (see equations (A-24) to (A-27) and equations (A-30) to (A-33)).

Based on the derivatives of matrices \mathbf{S} and \mathbf{b} above, and solving equations (24)–(33), we obtain the partial derivatives of the reflection coefficients and then the Fréchet derivatives.

References

- Aki, K., Richards, P.G., 1980. Quantative Seismology: Theory and Methods. Earth Science Reviews, New York.
- Auger, E., Virieux, J., Zollo, A., 2003. Locating and quantifying the seismic discontinuities in a complex medium through the migration and AVA analysis of reflected and converted waves: an application to the Mt Vesuvius volcano. *Geophys. J. Int.* 152 (2), 486–496.
- Ba, J., Xu, W., Fu, L., Carcione, J.M., 2017. Rock anelasticity due to patchy-saturation and fabric heterogeneity: A double double-porosity model of wave propagation. *Journal of Geophysical Research-solid earth* 122 (3), 1949–1976.
- Booth, D.C., Crampin, S., 1983. The anisotropic reflectivity technique: theory. *Geophys. J. Int.* 72 (3), 755–766.
- Carcione, J.M., 1997. Reflection and transmission of qP-qS plane waves at a plane boundary between viscoelastic transversely isotropic media. *Geophys. J. Int.* 129 (3), 669–680.
- Carcione, J.M., 2000. A model for seismic velocity and attenuation in petroleum source rocks. *Geophysics* 65, 1080–1092.
- Carcione, J.M., 2014. *Wave Fields in Real Media. Theory and Numerical Simulation of Wave Propagation in Anisotropic, Anelastic, Porous and Electromagnetic Media.* Elsevier.
- Carcione, J.M., Helle, H.B., Avseth, P., 2011. Source-rock seismic-velocity models: gassmann versus Backus. *Geophysics* 76, N37–N45.
- Chen, Y., Bai, M., Chen, Y., 2019. Obtaining free USArray data by multi-dimensional seismic reconstruction. *Nature Communications* 10 (1), 1–13.
- Chen, Y., Chen, X., Wang, Y., Zu, S., 2019. The interpolation of sparse geophysical data. *Surv. Geophys.* 40, 73–105.
- Daley, P.F., Hron, F., 1977. Reflection and transmission coefficients for transversely isotropic media. *Bull. Seismol. Soc. Am.* 67, 661–675.
- Daley, P.F., Hron, F., 1979. SH waves in layered transversely isotropic media—an asymptotic expansion approach. *Bull. Seismol. Soc. Am.* 69 (3), 689–711.
- Dębski, W., Tarantola, A., 1995. Information on elastic parameters obtained from the amplitudes of reflected waves. *Geophysics* 60 (5), 1426–1436.
- Ding, P., Wang, D., Di, B., Li, X., 2019. Investigation of the effects of fracture orientation and saturation on the Vp/Vs ratio and their implications. *Rock Mech. Rock Eng.* 52 (9), 3293–3304.
- Fatti, J.L., Smith, G.C., Vail, P.J., Strauss, P.J., Levitt, P.R., 1994. Detection of gas in sandstone reservoirs using AVO analysis: a 3-D seismic case history using the Geostack technique. *Geophysics* 59 (9), 1362–1376.
- Fryer, G.J., Frazer, L.N., 1984. Seismic waves in stratified anisotropic media. *Geophys. J. Int.* 78 (3), 691–710.
- Graebner, M., 1992. Plane-wave reflection and transmission coefficients for a transversely isotropic solid. *Geophysics* 57 (11), 1512–1519.
- Grechka, V., Tsvankin, I., Bakulin, A., Hansen, J.O., Signer, C., 2002. Joint inversion of PP and PS reflection data for VTI media: a North Sea case study. *Geophysics* 67 (5), 1382–1395.
- Guo, Q., Ba, J., Luo, C., Xiao, S., 2020. Stability-enhanced prestack seismic inversion using hybrid orthogonal learning particle swarm optimization. *J. Petrol. Sci. Eng.* 192, 107313.
- Guo, Q., Zhang, H., Cao, H., Xiao, W., Han, F., 2020. Hybrid seismic inversion based on mult-order anisotropic Markov random field. *IEEE Trans. Geosci. Rem. Sens.* 58 (1), 407–420.
- Hale, D., 2009. A method for estimating apparent displacement vectors from time-lapse seismic images. *Geophysics* 74 (5), V99–V107.
- Huang, G., Chen, X., Luo, C., Chen, Y., 2020. Geological Structure-Guided Initial Model Building for Prestack AVO/AVA Inversion. *IEEE Trans. Geosci. Rem. Sens.* <https://doi.org/10.1109/TGRS.2020.2998044>.
- Huang, G., Chen, X., Luo, C., Li, X., 2019. Pre-stack waveform inversion by using optimized linear inversion scheme. *IEEE Trans. Geosci. Rem. Sens.* 57 (8), 5716–5728.
- Karimpouli, S., Malehmir, A., 2015. Neuro-Bayesian facies inversion of prestack seismic data from a carbonate reservoir in Iran. *J. Petrol. Sci. Eng.* 131, 11–17.
- Kennett, B.L.N., 1983. *Seismic Wave Propagation in Stratified Media*, Advances in Applied Mechanics. Cambridge University Press.
- Kennett, B.L.N., Kerry, N.J., 1979. Seismic waves in a stratified half space. *Geophys. J. Int.* 57 (3), 557–583.
- Lee, H., Koo, J., Min, D., Kwon, B., Yoo, H., 2010. Frequency-domain elastic full waveform inversion for VTI media. *Geophys. J. Int.* 183 (2), 884–904.
- Li, K., Yin, X., Zong, Z., 2017. Pre-stack Bayesian cascade AVA inversion in complex-Laplace domain and its application to the broadband data acquired at East China. *J. Petrol. Sci. Eng.* 158, 751–765.
- Li, T., Mallick, S., 2013. Prestack Waveform Inversion of Four-Component, Two-Azimuth Surface Seismic Data for Orthorhombic Elastic Media Parameters Using a Nondominated Sorting Genetic Algorithm. *SEG Technical Program Expanded Abstracts*.
- Li, T., Mallick, S., 2015. Multicomponent, multi-azimuth pre-stack seismic waveform inversion for azimuthally anisotropic media using a parallel and computationally efficient non-dominated sorting genetic algorithm. *Geophys. J. Int.* 200 (2), 1136–1154.
- Liu, Q., Dong, N., Ji, Y., Chen, T., 2018. Direct reservoir property estimation based on prestack seismic inversion. *J. Petrol. Sci. Eng.* 171, 1475–1486.
- Lu, J., Yang, Z., Wang, Y., Shi, Y., 2015. Joint PP and PS AVA seismic inversion using exact Zoeppritz equations. *Geophysics* 80 (5), R239–R250.
- Lu, J., Wang, Y., Chen, J., An, Y., 2018. Joint anisotropic amplitude variation with offset inversion of PP and PS seismic data. *Geophysics* 83 (2), N31–N50.
- Luo, C., Li, X., Huang, G., 2018. Information on S-Wave Velocity and Density Obtained from Multi-Wave Data. *SEG Technical Program Expanded Abstracts*.
- Luo, C., Li, X., Huang, G., 2019. Pre-stack AVA inversion by using propagator matrix forward modeling. *Pure Appl. Geophys.* 176 (10), 4445–4476.
- Mallick, S., Adhikari, S., 2015. Amplitude-variation-with-offset and prestack waveform inversion: a direct comparison using a real data example from the Rock Springs Uplift, Wyoming, USA. *Geophysics* 80 (2), B45–B59.
- Mallick, S., Frazer, L., 1990. Computation of synthetic seismograms for stratified azimuthally anisotropic media. *J. Geophys. Res.* 95, 8513–8526.
- Padhi, A., Mallick, S., 2013. Accurate estimation of density from the inversion of multicomponent prestack seismic waveform data using a nondominated sorting genetic algorithm. *Geophysics* 32 (1), 94–98.
- Padhi, A., Mallick, S., 2014. Multicomponent pre-stack seismic waveform inversion in transversely isotropic media using a non-dominated sorting genetic algorithm. *Geophys. J. Int.* 5 (3), 589.
- Pan, X., Zhang, G., Cui, Y., 2020. Matrix-fluid-fracture decoupled-based elastic impedance variation with angle and azimuth inversion for fluid modulus and fracture weaknesses. *J. Petrol. Sci. Eng.* 189, 106974.
- Plessix, R., Bork, P., 2000. Quantitative estimate of VII parameters from AVA responses. *Geophys. Prospect.* 48, 87–108.
- Rüger, A., 1997. P-wave reflection coefficients for transversely isotropic models with vertical and horizontal axis of symmetry. *Geophysics* 62, 713–722.
- Rüger, A., 1998. Variation of P-wave reflectivity with offset and azimuth in anisotropic media. *Geophysics* 63 (3), 935–947.
- Rüger, A., 2002. Appendix A. Linearized VTI Scattering Coefficients, Reflection Coefficients and Azimuthal AVO Analysis in Anisotropic Media: *SEG Geophysical Monographs*, pp. 163–170.
- Smith, G.C., Gidlow, P.M., 1987. Weighted stacking for rock property estimation and detection of gas. *Geophys. Prospect.* 35 (9), 993–1014.
- Stovas, A., Ursin, B., 2003. Reflection and transmission responses of layered transversely isotropic viscoelastic medium. *Geophys. Prospect.* 51 (5), 447–477.
- Schoenberg, M., 1983. Reflection of elastic waves from periodically stratified media with interfacial slip. *Geophys. Prospect.* 31 (2), 265–292.
- Shuey, R.T., 1985. A simplification of the Zoeppritz equations. *Geophysics* 50 (4), 609–614, 1985.

- Thomsen, L., 1986. Weak elastic anisotropy. *Geophysics* 51 (10), 1954–1966.
- Thomsen, L., 1993. Weak elastic anisotropy. In: Castagna, J., Backus, M. (Eds.), *Offset-Dependent Reflectivity: Theory and Practice of AVO Analysis*. Society of Exploration Geophysicists.
- Ursin, B., Haugen, G.U., 1996. Weak-contrast approximation of the elastic scattering matrix in anisotropic media. *Pure Appl. Geophys.* 148 (3), 685–714.
- Veire, H.H., Landrø, M., 2006. Simultaneous inversion of PP and PS seismic data. *Geophysics* 71 (3), R1–R10.
- Vavryčuk, V., Pšenčík, I., 1998. PP-wave reflection coefficients in weakly anisotropic elastic media. *Geophysics* 63 (6), 2129–2141.
- Vavryčuk, V., 1999. Weak-contrast reflection/transmission coefficients in weakly anisotropic elastic media: P-wave incidence. *Geophys. J. Int.* 138, 553–562.
- Wang, B., Chen, X., Li, J., Cao, J., 2016. An improved weighted projection onto convex sets method for seismic data interpolation and denoising. *IEEE Journal of Selected Topics in Applied Earth Observations and Remote Sensing* 9 (1), 228–235.
- Wright, J., 1987. The effects of transverse isotropy on reflection amplitudes versus offset. *Geophysics* 52 (4), 564–567.
- Zhang, F., Dai, R., Liu, H., 2015. High order approximation for scattering matrix in layered elastic medium and its application in pre-stack seismic inversion. *J. Petrol. Sci. Eng.* 131, 210–217.
- Zhang, F., 2017. Estimation of anisotropy parameters for shales based on an improved rock physics model, part 2: case study. *J. Geophys. Eng.* 14, 238–254.
- Zhang, F., 2019. A modified rock physics model of overmature organic-rich shale: application to anisotropy parameter prediction from well logs. *J. Geophys. Eng.* 16, 92–104.
- Zhang, F., Qian, K., Li, X., 2017. Estimation of anisotropy parameters for shales based on an improved rock physics model, part 1: theory. *J. Geophys. Eng.* 14, 143–158.
- Zhang, G., Yin, X., Zong, Z., 2019b. Nonlinear elastic impedance inversion in the complex frequency domain based on an exact reflection coefficient. *J. Petrol. Sci. Eng.* 178, 97–105.
- Zhang, F., Zhang, T., Li, X., 2019a. Seismic amplitude inversion for the transversely isotropic media with vertical axis of symmetry. *Geophys. Prospect.* 67 (9), 1–18.
- Zhi, L., Chen, S., Li, X., 2016. Amplitude variation with angle inversion using the exact Zoeppritz equations—theory and methodology. *Geophysics* 81 (2), N1–N15.